MEMS HERMETIC PACKAGING FOR EXTREMELY SENSITIVE ACCELEROMETERS WITH IN-PACKAGE PRESSURE SENSING SOLUTION

by

Yuxi Zhang

B.E., Zhejiang University, 2012

Thesis Submitted in Partial Fulfillment of the

Requirements for the Degree of

Master of Applied Science

in the

Department of Mechatronic System Engineering

Faculty of Applied Science

© **Yuxi Zhang 2016**

SIMON FRASER UNIVERSITY

Summer 2016

Approval

Name:	**Yuxi Zhang**
Degree:	**Master of Applied Science (Applied Science)**
Title:	***MEMS HERMETIC PACKAGING FOR EXTREMELY SENSITIVE ACCELEROMETERS WITH IN-PACKAGE PRESSURE SENSING SOLUTION***

Examining Committee: **Chair:** Amr Marzouk
Lecturer

Behraad Bahreyni
Senior Supervisor
Associate Professor

_____

Albert Leung
Supervisor
Professor

_____

Edward Park
Internal Examiner
Professor
School of Mechatronic System
Engineering

_____

Date Defended: June 10th 2016

Abstract

In Micro-Electro-Mechanical Systems packages, sealing pressure is one of the most important indicators of packaging quality. Traditional hermeticity testing methods are expensive and inconvenient. Solution for in-package pressure monitoring has long been appealing. Pirani sensor is a commonly used pressure sensor that can be integrated into Micro-Electro-Mechanical Systems packages. Our team is developing a hermetic packaging process for extremely sensitive and low noise accelerometers. A eutectic package sealing process is developed and evaluated. To verify the stability of environment inside the package, a low-cost, process flow compatible, space saving bondwire Pirani sensor has been explored. The sensing principle is based on resistance change of the filament is a function of pressure under constant electrical power. The feasibility of using the bondwire Pirani sensor has been thoroughly discussed. A novel four point measurement set up is implemented to achieve the accurate low resistance measurement. The bondwire Pirani sensor has a dynamic range from 0.1 $Torr$ to about 50 $Torr$ and is compatible with any micro-system such as resonators, gyroscopes, micro-mirrors, and micro-display systems among others. The sensor is applied to our own packaging process as pressure sensing element to detect pressure change. Long-term pressure stability for sealed packages is also measured by the bondwire Pirani sensor.

Keywords: Pirani sensor; MEMS hermetic packaging; zero cost; in-package pressure monitoring

Acknowledgements

Foremost, I would like to express my deepest gratitude to my research supervisor, Prof. Behraad Bahreyni, for his encouragement, guidance and support during my graduate studies and research. I appreciate his patience, enthusiasm, and motivation. Without his help, this thesis would not have been possible.

I am thankful to Prof. Albert Leung, who has provided guidance and assistance during my research, especially in discussing the research idea and formulating the problem.

Special thanks to Amin Rasouli for his expertise in microfabrication and his precious assistance in my research. My sincere thanks also go to colleagues in our research group for sharing their knowledge and to all my friends who encouraged and supported me during my graduate studies.

This work was supported in part by the Natural Sciences and Engineering Research Council (NSERC).

Last but not least, I would like to express my gratitude to my beloved parents for their encouragement, support and greatest love of all. To them, I dedicate this thesis.

Table of Contents

List of Tables

List of Figures

Chapter 1

Introduction

This chapter gives an introduction of Micro-Electro-Mechanical Systems (MEMS) hermetic packaging approaches and pressure sensing solutions. The first section briefly introduces the background for this research. The second section talks about MEMS hermetic packaging. This is followed by the third section, which is the pressure sensor part. Motivations of this research will be discussed in the fourth section. And an outline of this thesis will be the last section.

1.1   Background

Micro-Electro-Mechanical Systems consist of mechanical and electrical parts fabricated at micro-scales. Packaging is a critical process for MEMS devices. The purpose of MEMS packages is to not only give MEMS devices physical support but also keep a reliable internal environment for better performance. As an important indicator of stability of internal environment, measurement of the pressure inside a package has been attracting researchers' attention.

Our team is developing extremely sensitive and low-noise accelerometers in collaboration with an industrial partner. These devices ought to measure sub-μg level accelerations in the frequency band of 50 Hz to 5 kHz. Because of the noise and size limitations, these sensors should be operated under partial vacuum of about 5-50 $Torr$ to reduce the noise generated through viscous damping. Therefore, a customized hermetic packaging procedure needs to be developed for our sensors. In order to know whether the pressure inside package is stable or not, an in-package pressure sensing solution is also appealed.

1.2   MEMS Packaging

Unlike IC packages, MEMS packages need to provide some level of access to the environment for sensing purposes. Due to the complexity and variety of MEMS devices, MEMS packaging process is device specific. However, IC packaging developments can sometimes be implemented to the MEMS world.

Several concerns need to be addressed for MEMS packaging including mechanical support, protection from the environment, interconnections, space and cost.

- Mechanical support: the core functioning part of a MEMS device is always mechanical. Thus, to protect those fragile moving parts from physical damage, a solid mechanical support is preferred.

- Protection from the environment: though not a necessity, most MEMS devices will benefit from being hermetically sealed in a package. For one thing, a better Q-factor can improve many MEMS devices' performance such as resonators and gyroscopes. A package further protects the devices from moisture damage, dust and so on. [14].

- Interconnections: interconnections consist of two parts. One is the feed-through for interfacing the device with outside world. This part is usually already completed by the commercial packages for MEMS. Conductive paths are created by metal plated pads. The other interconnection is the access to measurand. Since the signal that a MEMS device is supposed to measure can be physical, chemical or biological, i.e. pressure or flow rate, this may lead to an even more complicated package design.

- Space and cost: these two factors have a strong correlation. A more compact package design is always prevalent to those redundant ones and means less cost. For a given device, the size of a package depends on the size of the device as well as specific device-wise requirements. Actually packaging cost can sometimes rival the cost of device itself.

In general, wafer-level packaging (WLP) and chip-level packaging (CLP) are two typical types of MEMS packaging techniques. WLP uses batch fabrication to cap the MEMS devices before dicing, which gives the devices sealed cavities [15], while CLP do the sealing process after each device is diced and released. Although WLP seems more efficient and cost effective, CLP is still the main packaging process especially for research based MEMS. Different kinds of packages are available for CLP including metal packages, ceramic packages, plastic packages, etc.

We have chosen the 44 pin ceramic Leadless Chip Carrier as our package as it has large cavity and enough pin counts as well as good performance in terms of hermetic packaging.
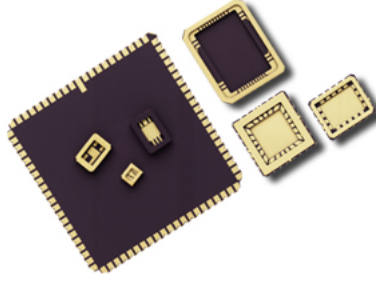
Figure 1.1: Ceramic Leadless Chip Carriers (Courtesy: Spectrum.Inc).

Shown in Fig. 1.1. Leadless Chip Carrier (LCC) Package is a long established standard industry package. This surface mount package consists of a co-fired ceramic base that has metalized terminals/pads on the sides and bottom of the package. LCC package has terminals/pads on all four sides of the package. The lid for this package can be either ceramic "frit sealed" or metal "solder sealed". This package provides a hermetic environment for the chip inside. LCC can be soldered directly to a printed circuit board (PCB) or used in a socket for testing. Furthermore the coefficient of thermal expansion (CTE) of the package is close to that of silicon die to minimize the stress produced during packaging steps. The pin count for the package is more than sufficient for our accelerator's electrical connections and the size is relatively compact. Our main concern about the packaging process focused on pressure stability and size.

1.3   Pressure Monitoring Solution

To verify the stability of pressure inside a sealed package, pressure sensing element can be integrated into the microsystem. Plenty of MEMS pressure sensors are available out there. Amongst these sensors, Pirani sensor can be a robust choice. It was first invented by Italian Marcello Pirani in 1906. The sensor operates based on the physical principle that gas thermal conductivity can be affected by the density of the ambient gas molecules [13]. For a simple model, one wire coil is used as a heater, and another is used as a sensing probe, both of which are put in the same cavity. When the gas density in the cavity changes, the heat transferred between the two filaments by gas molecules will change correspondingly. Since gas density is a function of pressure, pressure can be inferred from the amount of heat transfer.

As MEMS has been extensively applied in many fields, the concept Pirani sensor was also introduced into the MEMS world – giving rise to many kinds of micromachined Pirani sensors. With the help of microfabrication, the size of a sensor shrinks to μm scale. That

brings out many advantages over the conventional Pirani gauges such as low cost and fast response.

In this thesis two kinds of Pirani gauge designs were demonstrated. A batch of silicon based sensor designs were simulated, fabricated and tested. The device length, width and thickness is 150 μm, 5 μm and 2 μm and gap between device and bottom heat sink is 0.8 μm. However, due to device integration issues and application space limitation, we were forced to find another way out, which will be discussed in detail in Section. 1.4. Another solution is presented as fast and space saving, almost at zero cost pressure sensing element: bondwire Pirani sensor. The sensor can be formed easily with a wire bonding machine. The diameter of the wire is flexible and available in the market from 12.5 μm to 50 μm. In order to measure the small resistance of these wires, in-package four point measurement was implemented. With a simple set up, we get rid of the complicated probe station measurement. It also makes measuring the pressure of a vacuum sealed package possible. One of its significant advantages over the traditional silicon Pirani sensors is that it can be integrated into any MEMS package regardless of the type of the device.

1.4 Motivations

Although there have been many designs of MEMS pressure sensors available for detecting different pressure ranges, MEMS package pressure sensing has long been challenging in some applications due to many reasons:

- For testing the hermeticity of a sealed package, a traditional way is to use Helium leak testing and Q factor extraction [16, 17]. However, Helium leak testing expensive and can not achieve in-situ and real time measurement. On the other hand Q factor measurement cannot resolve small pressure changes due to material instability [18]. Therefore integrating a proper pressure sensing element into MEMS package was considered to be highly regarded.

- There are commercial Pirani sensors out there which have outstanding detection performance. However, they are fairly expensive for individual users and even for industrial users. The cost of a dedicated single sensor chip could be as much as about $3000 Canadian [19]. Even if setting aside the cost issue, the sensor itself will take about 2 mm × 2 mm space. Extra labour is required for attaching them solidly in a carrier.

- Designing and integrating our own Pirani sensor to each device design layout seems to be a feasible approach. A number of silicon based Pirani sensors were designed and tested . They function well under proper operation. But once again, they will take up a certain amount of space on MEMS device chip, which could already have

been tight. Moreover, adding this part to device layout may lead to a higher failure rate of microfabrication process. Once they fail there is no longer any opportunity of knowing the pressure signal for that device. To avoid this kind of issue, some spare pressure sensors will also be included on device chip, which will make space on the chip even more compact.

One main issue about this approach is its applicability among different devices and packages. Thus, the pressure sensor must rely on the same process flow as the MEMS device it is going to be integrated with. So it means the design will be changed from time to time depends on different application. In some cased it might be impossible to integrate such pressure sensing element to the chip.

1.5 Structure of the Thesis

Chapter. 2 presents the related works in MEMS hermetic packaging as well as in-package pressure sensing. Chapter. 3 describes the working mechanism of Pirani sensor, followed by our sensor designs. In chapter. 4, our hermetic packaging process flow is discussed with some information about our vacuum packaging system. Chapter. 5 provides our experimental results for both sensor characterizing and hermetic sealing. Conclusion and future work are discussed in the last Chapter.

Chapter 2

Literature review

This chapter presents the related works in the field of MEMS packaging as well as in-package pressure sensing. A few examples are given to help explaining each technique. Throughout the review the rationality of utilizing each technology to our application is also discussed specifically.

2.1 MEMS Packaging Techniques

MEMS packaging techniques are influenced by the IC packaging technology. With the rapid growth in the segment, the need of finding cost-effective packaging solutions becomes more and more important. The evolution of MEMS packaging mostly focused on cost, performance and reliability [20]. MEMS packaging techniques mainly have two categories, namely Wafer Level Packaging (WLP) and Chip Level Packaging (CLP). Each packaging technique has its own pros and cons as mentioned in Section. 1.2.

For WLP, a wafer-to-wafer bonding process is often required. The bonding can be categorized into direct bonding, anodic bonding and bonding with intermediate layers [21]. Nowadays, bonding with intermediate layers becomes dominant in wafer-to-wafer bonding. The most used material for the intermediate layer is solder such as Au/Sn or glass frits.

In 2007, F. Theunis et al. from NXP Semiconductors showed a novel and efficient wafer level capping technology for RF-MEMS devices [22]. Their method is based on silicon cap using Au/Sn bond in order to create a hermetic seal. Three lithography steps were applied to manufacture the cap wafer. 6" wafer level wafer-to-wafer bond was achieved in their technology. Since measuring the hermeticity level using standard fine leak test method inside such small cavity is impossible, they conducted a destructive measuring method by keeping the sealed cavity in high pressure target gas environment and measuring the amount of gas forced in. Au/Sn eutectic bonding is also a popular technology in WLP. In
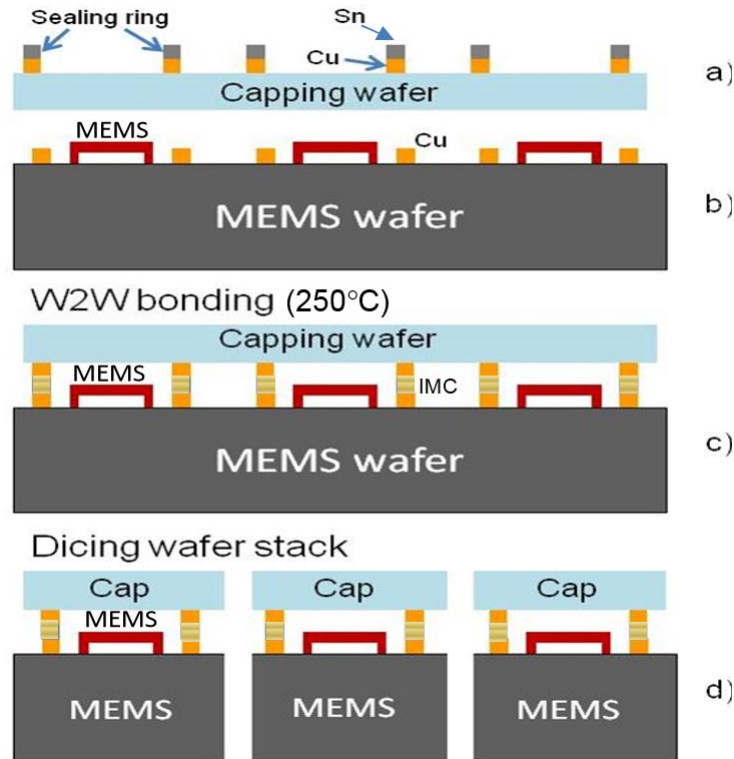
Figure 2.1: Chip capping technology flow relying on CuSn/Cu bonding metallurgy. a) capping wafer with Cu/Sn sealing ring; b) the MEMS wafer waiting for capping; c) wafer to wafer bonding; d) device dicing after encapsulation © IEEE 2010 [2].

A. Garnier's study [23], a Ni layer was used to react with solder material to realize a nearly void free joint.

Besides Au/Sn, other materials are also used for WLP. In 2010, Nga P. Pham et al. used a double layer Cu/Sn as bond frame to create hermetic seal for MEMS wafer [2]. Fig. 2.1 shows the process flow of their work. The enclosed bond was composed of Cu-Sn and electro-deposited in a resist plating mould. And Cu ring was electroplated on MEMS wafer. Then the two wafers were bonded together and diced. Membrane deflection method leak testing and tensile testing were conducted to prove the quality of seal.

Another example of WLP is the fabrication and characterization process for a wafer level package reported by Junseok Chae et al. in 2008 [3]. The schematic view of the package is shown in Fig. 2.2. The substrate was made of standard thickness glass. Vertical feedthroughs were fabricated using wet etching. The cap of package was made of silicon or glass. A Pirani gauge was integrated inside the package to characterize the vacuum package.
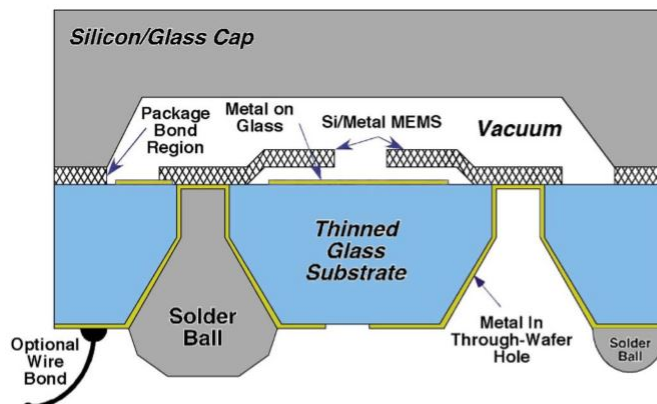
Figure 2.2: Structure of a typical wafer level package reported by Junseok Chae et al. © IEEE 2008 [3].

Sometimes, MEMS devices such as chemical sensors require access to the ambient for sensing the measurand. In these cases it could be tricky to handle possible damage and contamination caused by open access especially when under harsh environments. In 2011, Robert Neal Dean et al. demonstrated a die carrier fabricated by screen printing electrical traces onto a porous ceramic substrate [4]. As shown in Fig. 2.3, a thick porous ceramic substrate serves as both the substrate carrier and the filter for humidity sensor underneath. Moist air can flow through the substrate to the sensor while dust and other contaminations are shielded by the filter.

Using WLP can reduce the packaging cost which is considered to be the most expensive part for MEMS devices' process flow. However, this advantage can only be seen when there is a mature manufacturing line to ensure a stable yield. That also means the devices for packaging should have reliable performance.

The aforementioned aspects destine that for our project CLP is a better choice. As our accelerometer is still under designing phase for research use, both the quantity and the reliability of the devices are not sufficient to choose WLP. CLP is definitely a more compatible choice at this stage. Moreover, the devices' layouts are subject to change, which will make the WLP process design even more unpredictable. Last but not least, WLP take place before chip dicing. After sealed it is harder for design team to figure out the cause of failure for tested devices. This step is especially essential in a research.

CLP, also called discrete packaging, often uses metal, ceramic or plastic chip carriers to hold MEMS device chips. A traditional CLP process consists of 4 steps: die attaching, wire bonding, sealing and testing. Device attachment can be done by glue or bonding, depending

8
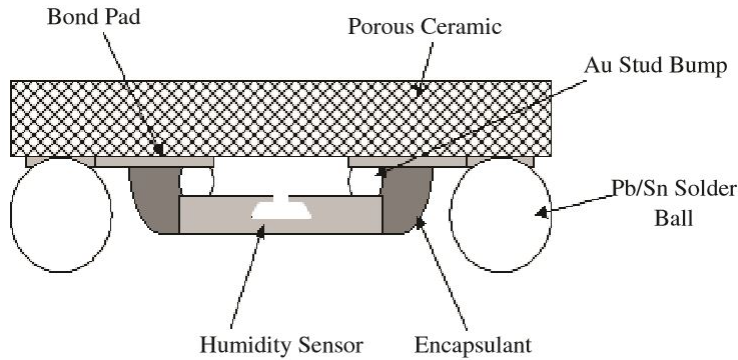
Figure 2.3: Illustration of the porous ceramic substrate packaging concept © IEEE 2011 [4].

on the application. There are many choices to make such as the type of package, cover and die attachment material that may lead to different trade offs.

For choosing the type of package, many aspects shall be taken into consideration. First is the material of chip carrier. Different chip carrier has different benefits in terms of hermeticity, cost, and dimensional requirements. The second is the size of the chip carrier: it not only depends on the size of MEMS device, but also the number of electrical connections needed which will affect the pin count of chip carrier. Currently there are several kinds of packages available which are adapted from IC industry:

- Metal packages: the most expensive package. They satisfy pin count requirements for most applications and are relatively compact.

- Plastic packages: low cost, low weight. But its absorbing moisture makes it a bad choice for hermetic packaging.

- Ceramic packages: medium cost. These packages are proved to be the preferred choice for MEMS chip level hermetic packaging.

The use of ceramic packages for MEMS devices is common nowadays. In 2003, researchers attempted to use Au80/Sn20 solder to seal a MEMS structure with ceramic quad flatpack (CQFP) [5]. To avoid the thermally-induced damage and stress-pattern-changes in MEMS devices caused by global heating during packaging process, they developed a CO_2 laser-assisted silicon lid encapsulation process for ceramic packages. Schematic of packaging is shown in Fig. 2.4. Their results showed a helium leak rate of below 10^{-8} $atm\ cc/s$. However, it is almost guaranteed that the chip carrier, especially the off-the-shelf ones, will have gas trapped on the surfaces inside the cavity. In such small cavity outgassing will be a
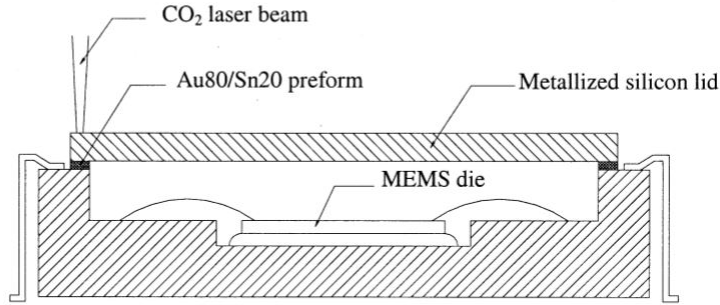
Figure 2.4: CO_2 laser-assisted silicon lid encapsulation © IEEE 2003 [5].

major problem in terms of pressure stability. A common approach is to solve this issue by a thoroughly baking before sealing [24, 25]. Baking cannot push the vacuum level further at some point. In order to get a better vacuum inside a sealed package, getters might be used to absorb residual gas. D. Sparks et al. presented the utilization of a multi-layer, thin-film NanoGetter [6]. The highlight of this research is that instead of putting nonevaporable getter (NEG) materials in an extra micromachined (Fig. 2.5) cavity adjacent to the sealed device cavity, a thin film getter was deposited on the etched cap wafer (Fig. 2.6). In that way, the chip size was maintained the same.

Therefore, under careful operation, using the off-the-shelf ceramic packages is also possible to meet the environment requirements for different levels of MEMS hermetic packaging. In terms of sealing the package, there are also plenty of choices. Anodic, fusion and polymer bonding are used for MEMS packaging. Amongst them Au/Sn solder alloy eutectic bonding seems to be feasible with its superior physical properties, as shown in Table. 2.1 [1]. In 2003, Seong-A Kim utilized a closed-loop AuSn solder-line bonding to a hermetic MEMS package [26]. This low temperature, high strength, high speed packaging process stands out as a good option for MEMS packaging. And if for some of the applications that temperature would be a main concern, ultrasonic bonding with for example indium-to-gold and aluminum-to-aluminum is also a possible solution [27, 28].

2.2   In-Package Pressure Monitoring

Measuring pressure has long been an interesting topic. From the hydrostatic gauges to micro-scale pressure sensors, pressure sensing elements are becoming smaller and more efficient, applicable to more and more situations. In this section, previous designs of micro pressure sensors are reviewed and compared.

10
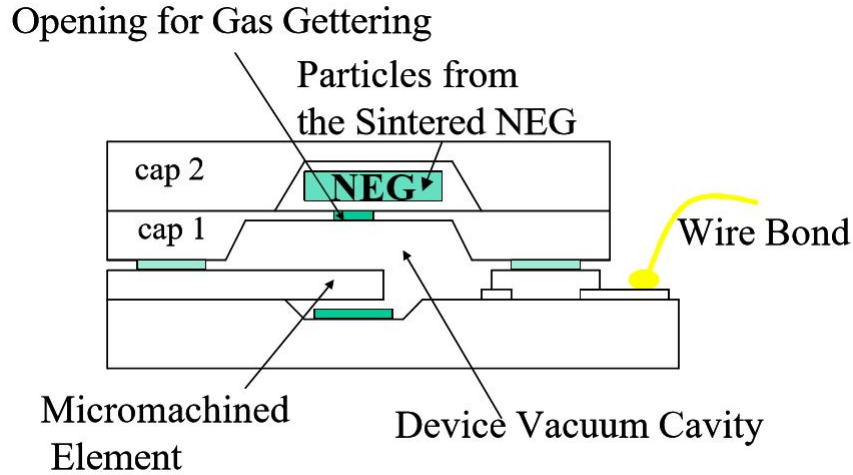
Figure 2.5: Conventional method of integrating getters to package using an isolated cavity © IEEE 2003 [6].
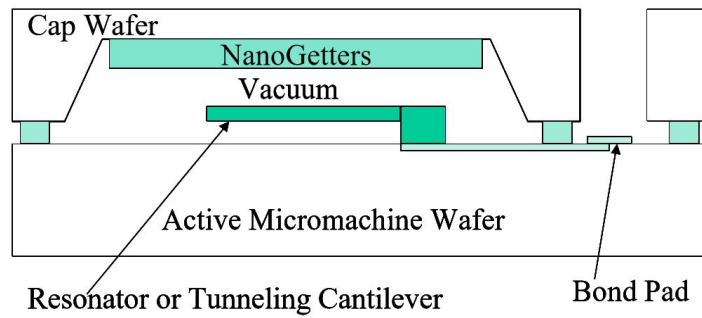
Figure 2.6: D. Sparks' getter integration using NanoGetter deposition © IEEE 2003 [6].

Table 2.1: Physical properties of Au/Sn alloy [1]

Properties	Value
Density	$14.7 \; g \cdot cm^{-3}$
Coefficient of thermal expansion	$16 \times 10^{-6}/^{\circ}C$
Thermal conductivity	$57 W \cdot m^{-1} \cdot K^{-1}$
Tensile strength	275 MPa
Young's modulus	68 GPa
Shear modulus	25 GPa
Poisson's ration	0.405
Electrical resistivity	$16.4 \times 10^{-8} \Omega \cdot m$
Elongation	2%

11
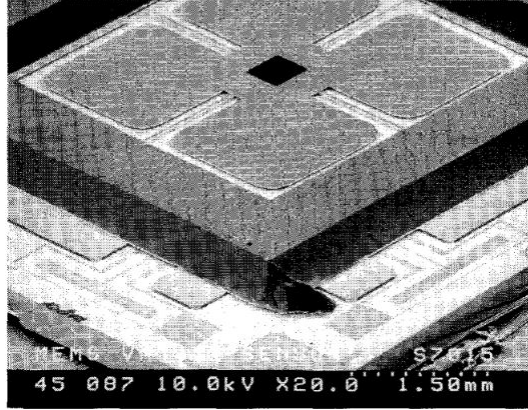
Figure 2.7: SEM picture of bulk micromachined pressure sensor © IEEE 1997 [7].

When considering micro-machined pressure sensors, many designs can fulfil the in-package pressure sensing task. Amongst all the sensors, diaphragm pressure sensors and thermal pressure sensors are the most commonly used ones. A typical diaphragm pressure sensor contains a flexible membrane which deforms when pressure is applied. The deformations are then measured by either piezo-resistive or capacitive methods, among others.

Back in 1997, Roman C. Gutierrez et al. presented a bulk micromachined resonance pressure sensor made of silicon [7]. Fig. 2.7 shows the SEM of the resonance vacuum sensor. The middle of the four leaf clover structure is the moving part which was suspended by four silicon anchors. The sensor was calibrated against a thermocouple gauge, a capacitance manometer, a spinning rotor gauge and a hot cathode ionization gauge. Its pressure sensitivity range was reported to be between $10^{-6} \, Torr$ to $10^{-1} \, Torr$.

One year later, Masayoshi et al. discussed several types of micromachined pressure sensors in their review [8]. One device is a capacitive vacuum sensor the gap of which was etched by TMAH, structure shown in Fig. 2.8. Room was also saved for NEG to absorb any remaining gas in the reference cavity. Different layers were fabricated and anodically bonded together. The working principle of this sensor is straight forward: since the reference cavity pressure is fixed, a different ambient pressure will push the moving part, which will cause the capacity changing correspondingly. The drawback of this sensor is the existence of reference cavity and complicated fabrication.

Another pressure sensor discussed was a microdiaphragm pressure sensor, as shown in Fig. 2.9. The moving diaphragm is formed by anisotropic etching. Deformation of the diaphragm was measured by polysilicon piezoresistors and translated to a pressure signal. This approach also needs a reference cavity and calibration process. Many of the later works were based these early works [29, 30].
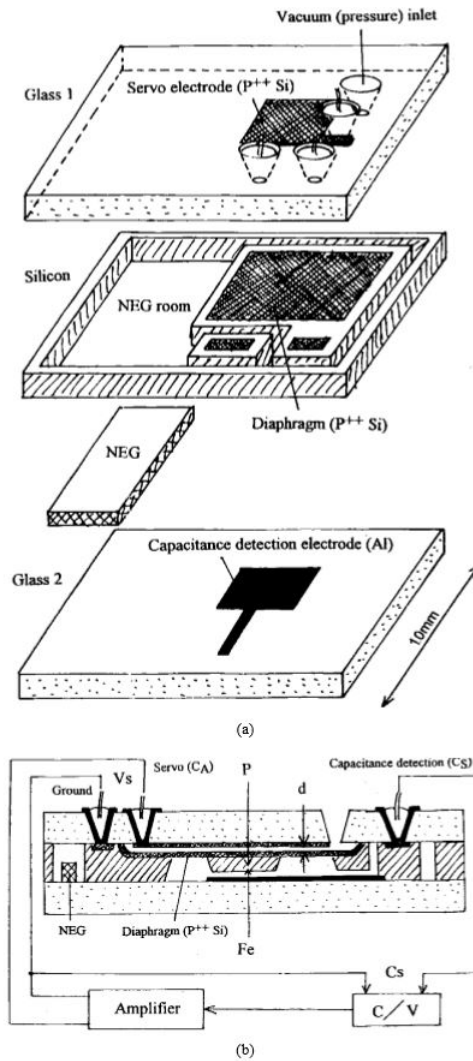
Figure 2.8: Schematic view of the capacitive vacuum sensor. Top shows different layers of the fabricated device; bottom shows the cross section view. © IEEE 1998 [8].
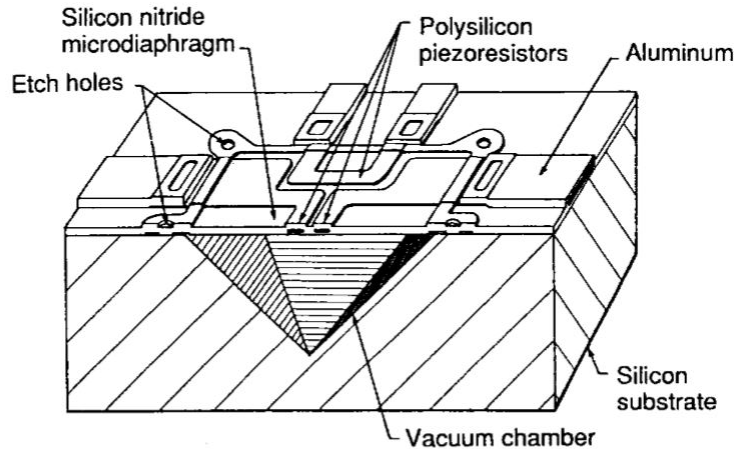
Figure 2.9: Schematic view of the microdiaphragm vacuum sensor © IEEE 1998 [8].

For these diaphragm pressure sensors, a discrete microfabrication step is always needed. The need for a reference cavity requires a careful calibration and may have pressure limit due to diaphragm structure. Therefore, as discussed in Section. 1.3. Pirani pressure sensors have many advantages over others in the field of in-package pressure monitoring.

In 1991, Mastrangelo thoroughly discussed the applications of electrically heated microbridges [31]. A few free-standing beams fabricated as integrated absolute gas-pressure sensors were demonstrated. Cross sections shown as Fig. 2.10. The beam is a few μm^2 in cross section and several hundred μm long. It was made of polycrystalline-silicon with silicon-nitride coat. The sensor was operated under constant temperature mode. A digital signal representative of the absolute pressure was also achieved. The measurement range of this microbridge is from 10 Pa (75 $mTorr$) to 10^4 Pa (75 $Torr$).

In 1999, BedoÂÍ et al. from Germany compared two different kinds of micromachined Pirani vacuum sensors: a planar and a sandwich structure under DC and AC measurement respectively [32].They are both Pt thin film resistors on top of silicon nitride membrane. Both structures are reported to be able to measure pressure between 10 μbar and 1 bar. Temperature modulation was used to increase the measurement range.

In 2003, Brian H. Stark et al. reported a doubly anchored surface micromachined Pirani gauge integrated into a sealed micro cavity for vacuum characterization [18]. The extra doubled anchors made great contribution to stiffen the membrane. As a result the sensitivity and dynamic range was substantially enhanced by the reliable fabrication of large area gauges and 800 nm thin gaps. The sensor was able to measure from 1 $mTorr$ to atmospheric with a 3 $\mu Torr$ resolution.

14
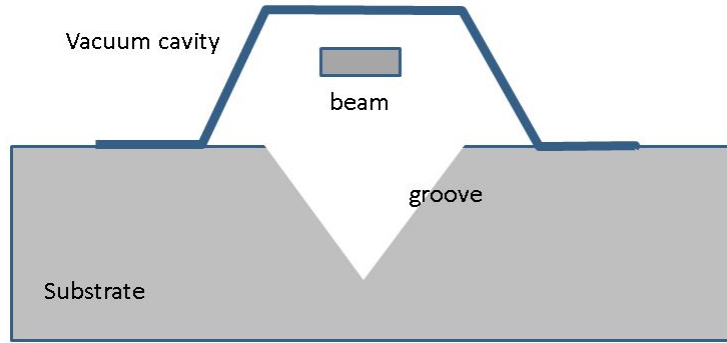
Figure 2.10: redraw cross sections of microbridges by Mastrangelo [9].

In 2005, Brian H. Stark et al. presented another surface micromachined poly beam Pirani gauge. It has a dynamic range from 10 $mTorr$ to greater than 760 $Torr$ with 1×10^3 $(K/W)/Torr$ sensitivity [33]. The highlight of that research is that the device's high performance is achieved by a foundry process. A combination of different devices with different dimensional parameters were used to guarantee wide dynamic range and high sensitivity.

Also in 2005, Junseok Chae, together with Brian H.Stark and Khalil Najafi, reported a micro Pirani gauge with dual heat sinks both at top and bottom side of the sensing beam. The sensor was integrated with MEMS devices inside a vacuum package to pressure stability in long-term [34]. The gaps between heat sinks and sensor were minimized to extend the lower end of dynamic range. The sensor has a dynamic range from 20 $mTorr$ to 2 $Torr$, with 3.5×10^5 $(K/W)/Torr$ sensitivity.

The same year, Jay Mitchell designed and fabricated a ladder-shape Pirani sensor (Fig. 2.11) which can achieve pressure detection lower bound of 10 mTorr [10]. The design is based on the principle that the longer the beam is, the better performance it can have as a Pirani sensor. However the fabrication success depends on structural rigidity. Adding short links between two parallel suspended beams can improve the maximum length of beams and have a better temperature distribution at the same time. The sensor was reported to be able to measure from 0.01 to 760 $Torr$.

In 2009, Ebru Sagiroglu Topalli et al. presented a meander silicon coil microfabricated as heater and silicon islands on each side to serve as heat sinks [11], shown in Fig. 2.12. Sensors fabricated with silicon-on-glass process had a sensitivity of 3.8×10^3 $(K/W)/Torr$ over $50 - 5000$ $mTorr$ range, while sensors fabricated with dissolved-wafer process achieved a sensitivity of 4.2×10^4 $(K/W)/Torr$ with a dynamic range of $20 - 2000$ $mTorr$. The
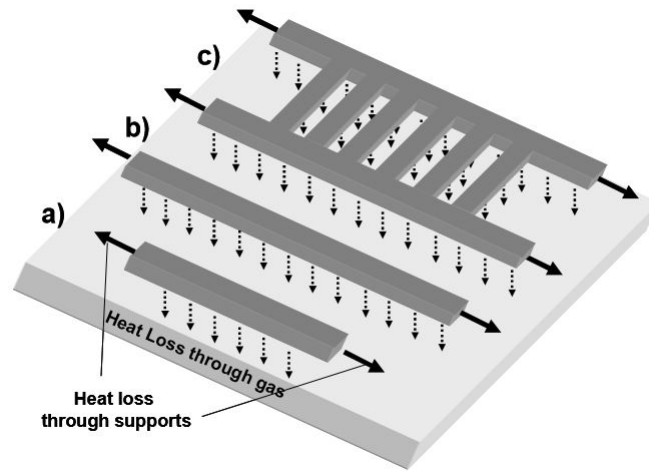
Figure 2.11: Schematic view of the ladder shape Pirani sensor: a) short bridge structure; b) long bridge structure; c) two long bridge structures with ladder shape support in between. © IEEE 2005 [10].
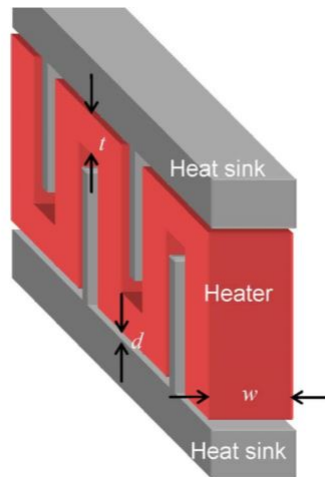
Figure 2.12: Schematic view of Ebru's meander Pirani sensor © IEEE 2009 [11].
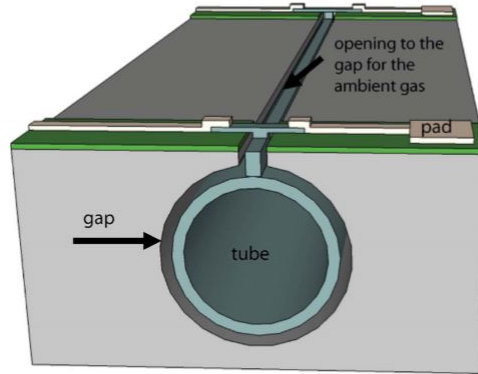
Figure 2.13: Sketch of the tube Pirani sensor © IEEE 2011 [12].

sensors were then put into vacuum-sealed hybrid platform packages to predict pressure inside microcavities.

In 2011, Fabio Santagata et al. presented a tube-shaped Pirani sensor buried in silicon substrate with very small footprint [12], as shown in Fig. 2.13. The shape of the sensor enabled 3-mm-long and 1.8-μm-thick tube sensor survived the fabrication process which yielded low detection limit. Tubes with different lengths were also tested and the result proves that increasing the length of the sensor can significantly push the lower bound of detection limit. The author also indicated that the results corresponded to their 1-D analytical model.

From 2009 to 2010, Yunsong Qiu, Yufeng Jin et al. from National Key Lab on Micro/Nano Fabrication Technology, Peking University have been working on mono-wire sensing unit [35, 36, 37]. A LTCC (Low Temperature Co-fired Ceramic) chip carrier was used as substrate to hold mono-wire sensor. Different materials such as Pt, Si-Al were compared and the relation between wire's dimension factors and sensing performance was discussed as well. The sensor was then supposed to monitor in packaging pressure. Dynamic range was reported to be 1 Pa (7.5 $mTorr$) to 1000 Pa (7.5 $Torr$).

As a special mention, this work is also inspired by one of our post-colleagues' work [38]. In 2007, Kourosh has demonstrated an innovative surface micromachined Pirani sensor. The sensor has an extreme narrow gap of 50 nm between the heater microbridge and the heatsink. The upper pressure range was increased to 650 kPa with significant sensitivity.

To sum up, regarding our application, Pirani sensor is a good solution due to its low fabrication and calibration complexity compared with diaphragm type pressure sensors. The sensor's dynamic range can cover our target range easily with simple sensor design.

Most important is that the design layout for Pirani sensors is flexible which enables a better integration score with other MEMS devices inside the package.

Chapter 3

Pressure sensing solution

In this Chapter, the basic concept and design concerns of a Pirani sensor were described. Simulation results are described for a couple of Pirani sensors. A novel in-package pressure sensing solution was presented. Bridge structure is formed by common bondwire by K&S 4700 Wire Bonder.

3.1 Basic Mechanism of Pirani Sensor

First invented by Italian Marcello Pirani in 1906, the famous Pirani sensor has found many useful applications in MEMS world. A conventional Pirani gauge contains two filaments, one as the heating part and the other as the sensing part, as shown in Fig. 3.1. The operation mechanism is based on thermal conductivity of gas is a function of gas pressure below a certain pressure range. The filament conducting constant power is heated in the cavity. Heat transfer between the heating filament and sensing filament is due to gas thermal conduction. At lower pressures, fewer gas molecules remain involved in this heat conduction process, which will lead to a lower temperature on the sensing filament. The resistance of
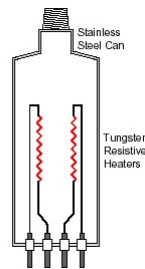
Figure 3.1: A typical set up of a conventional Pirani gauge [13].
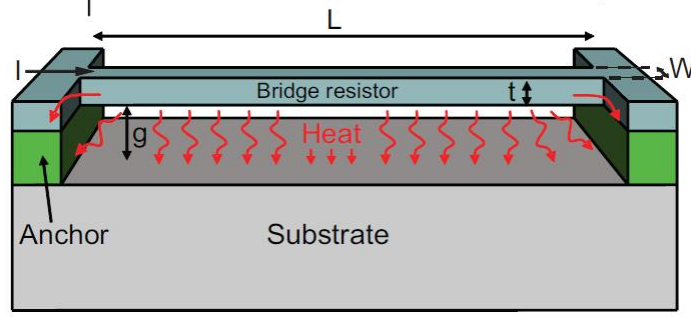
Figure 3.2: a bridge shape micro Pirani sensor © IEEE 2011 [12].

the filament change with its temperature accordingly. Hence, by measuring the resistance of the sensing filament, the pressure of gas in cavity can be calculated.

Another set up of Pirani sensor is becoming more common which combines the heating and sensing filaments into one, as shown in Fig. 3.2. The amount of heat transferred by gas molecules in between is proportional to pressure of gas (i.e. density of gas molecules). The less gas molecules exist, the hotter the filament will be at equilibrium. Thus, the final temperature of the heating filament is a measure of pressure level.

3.1.1 Analysis of A Bridge Micro Pirani Sensor

Pirani sensor is a kind of thermal pressure sensor. Talking about the fundamental heat transfer concepts before looking into Pirani sensor design is necessary. In nature, where there is temperature difference, there is heat transfer. The rate of this heat transfer is proportional to temperature gradient [39]:

$$q = -kA\frac{\partial T}{\partial x} \tag{3.1}$$

where q is the heat transfer rate, A is the cross section area and $\frac{\partial T}{\partial x}$ is the temperature gradient. Note the constant k is defined as "thermal conductivity", which is a fundamental property of materials. The unit for k is $W/m \cdot K$ [39].

When it comes to MEMS world, such simple mechanism will have incredible applications. Take a simple "bridge" structure Pirani sensor as an example to derive exactly how micro Pirani sensors work. As shown in Fig. 3.2, just like a traditional Pirani gauge, a micromachined bridge acts as the heater. When current passes through the bridge, as a resistor it will generate certain amount of heat.

There are three types of heat transfer: heat conduction, heat convection and radiation. In our case, the heat generated will be dissipated by: 1) heat conduction through the

20
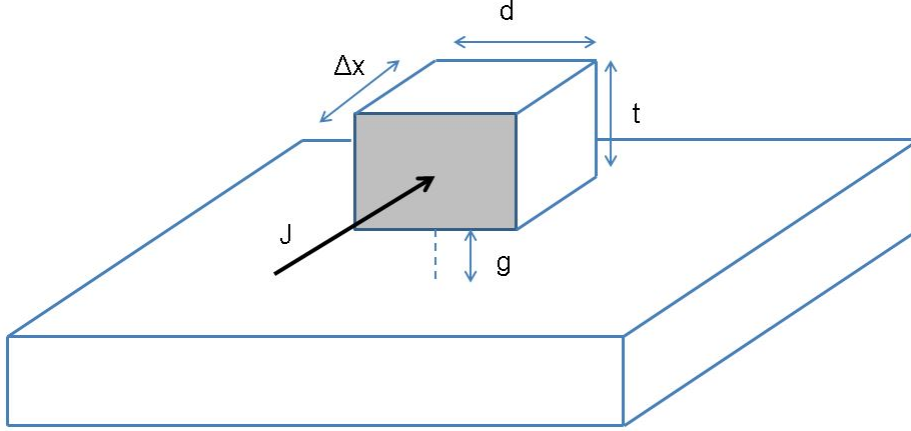
Figure 3.3: Differential element of bridge sensor.

anchors; 2) heat conduction by surrounding gas molecules; 3) heat convection by gas; 4) radiation to the environment. Consequently, the heat balance equation is:

$$Q_{total} = P_{gen} + Q_{cond} + Q_{conv} + Q_{rad} \tag{3.2}$$

where Q_{total} is the net rate of change of the internal energy and P_{gen} is the power generated in bridge.

If we take a differential element of the wire with Δx length, shown in Fig. 3.3, based on the dimension of the bridge, each term of the balance equation can be derived as follows:

$$P_{gen} = J^2 \rho_0 A \Delta x (1 + \alpha u(x)) \tag{3.3}$$

where J is the current density, ρ_0 is the resistivity of gold, A is the cross section area of the bridge, α is the TCR of material, and $u(x)$ is the temperature difference at point x before and after applying the current.

In Equation. 3.2, heat loss through conduction contains conduction by anchor and conduction by air. From Equation. 3.1, it can be derived as:

$$Q_{cond} = -k_b A \left(\frac{\partial u}{\partial x} \Big|_x - \frac{\partial u}{\partial x} \Big|_{x+\Delta x} \right) - k_g(P) \tau d \Delta x \frac{u(x)}{g} \tag{3.4}$$

where k_b and k_g are the thermal conductivity of bridge and gas, respectively. d is the diameter of the bridge and τ is a correlation factor. Therefore $\tau d \Delta x$ together makes the effective heat conduction area [9], g is the distance between bridge and substrate. Note that apparently $k_g(P)$ is a function of gas pressure.

The convection part can be derived based on Newton's cooling law:

$$Q_{conv} = 2h(\vartheta, P)A_{suf}u(x) \tag{3.5}$$

where $h(\vartheta, P)$ is the convective heat transfer coefficient. A_{sur} is the surface area of differential element. Radiation heat loss part can be ignored since the bridge will not be heated too much. Under steady state, take the limit of Δx to 0 and manipulate Equation. 3.2 - Equation. 3.5.

$$\frac{\partial^2 u}{\partial x^2} = \epsilon u - \delta \tag{3.6}$$

where $\epsilon = \frac{k_g(P)}{k_b}\beta\frac{1}{gt} - \delta\alpha + \frac{h(\vartheta,P)}{k_b}(\frac{1}{w} + \frac{1}{t})$ and $\delta = \frac{J^2\rho_0}{k_b}$

By solving the Equation. 3.6 a solution for $u(x)$ can be found as:

$$u(x) = \frac{\delta}{\epsilon}[1 - \frac{\cosh\sqrt{\epsilon}(x - \frac{L}{2})}{\cosh\sqrt{\epsilon}\frac{L}{2}}] \tag{3.7}$$

Here assume that the temperature of anchors and substrate are the same and they are stable. Then by taking the integral of $u(x)$ the resistance of bridge at equilibrium will be:

$$R_b = R_0[1 + \frac{\alpha\delta}{\epsilon}(1 - \frac{\tanh\sqrt{\epsilon}\frac{L}{2}}{\sqrt{\epsilon}\frac{L}{2}})] \tag{3.8}$$

In such small cavity like a MEMS package, convection can be negligible [40]. Therefore the effect of convection can be ignored. Then

$$\delta = I^2\frac{\rho_0}{A^2 k_b} \tag{3.9}$$

$$\epsilon = \frac{k_g(P)}{k_b}\beta\frac{1}{gt} - \delta\alpha \tag{3.10}$$

From above, consider Equation. 3.8, 3.9, 3.10, it is clear that given the same current and bridge size parameters, different ambient pressure P will lead to different $k_g(P)$. The value of ϵ will be affected as a result. Therefore the resistance of the bridge at equilibrium will be different.

3.1.2 Pressure Dependent Gas Thermal Conductivity

Note that in Equation. 3.10 the term $k_g(P)$ defines the thermal conductivity of gas, which links the pressure change to the temperature change of the microbridge. This section will focus on the characteristics of thermal conductivity of gas.

The thermal conductivity of gas is characterized by the dimensionless Knudsen number [41]:

$$K_n = \frac{\lambda}{d} \tag{3.11}$$

where λ is the Mean Free Path (MFP) of gas and d is the characteristic dimension of the domain. The MFP can be given as

$$\lambda = \frac{1}{\sqrt{2}\pi\sigma^2 n} \tag{3.12}$$

where $\pi\sigma^2$ is the collision cross section and n is the gas molecular density.

Based on value of Knudsen number, gas heat conduction can be divided into four distinct regimes:

- continuum regime for $K_n < 10^{-2}$;

- slip regime for $10^{-2} < K_n < 10^{-1}$;

- transition regime for $10^{-1} < K_n < 1$;

- molecular regime for $K_n > 1$.

In continuum regime, thermal conductivity of gas is independent of gas pressure and has a typical value of 0.026 $W/m \cdot K$. When the pressure enters transition regime, MFP becomes greater than d. Then the heat flux will be limited by the molecular collision rate, which is a function of gas density [9]. Therefore, at low pressure, thermal conductivity of gas becomes a function of gas pressure.

A commonly used expression for heat conductivity of gas is given by [9]

$$k_g(P) = k_c \frac{P}{P + P_0} \tag{3.13}$$

where P is the pressure of gas, k_c is the continuum limit and P_0 is the transition pressure.

Note that the empirical transition pressure P_0 is given by [9]

$$P_0 \approx \frac{2\tau d k_c T_g}{\pi \alpha_E \bar{\nu} dg} \tag{3.14}$$

At high pressure, intermolecular collisions are the main way of gas heat conduction in which case pressure does not seem to play an important role. In contrast with that, at the low pressure end because there is so few gas molecules exist to conduct heat, $k_g(P)$ is nearly zero. Adding the heat conduction by anchors to the total bridge heat conduction, the overall conductivity vs. pressure curve will be an "S" curve since at high pressure it

23

is almost constant while at low pressure under certain limit, heat conduction by anchors becomes dominant.

3.2   Micromachined Pirani Sensor

3.2.1   Design Considerations

In order to make the most use of package space and avoid the extra work load of separate fabrication and die handling, our goal is to design a process flow compatible Pirani sensor that could be integrated into any device design chip.

Equation. 3.4 indicates that the pressure of gas is only affecting the second portion of heat conduction which is the heat dissipated by the surrounding gas to the heat sink plate. Under constant power, heat conduction by the bridge anchors is independent of pressure and is almost constant. That is to say, now the target signal is the gas conduction part, and the anchor conduction portion is like the offset. In order to get a high strong signal, a very intuitive approach is to make the heat conduction by gas more efficient. For example, for the same cross section, the longer the bridge, the larger ratio of heat conducted by gas over heat conducted by anchors [10]. Hence, our goal was to have some innovative structural Pirani designs that can improve the heat dissipated by ambient gas.

3.2.2   Numerical Simulations

With the help of COMSOL Multiphysics [42], different Pirani designs were simulated using finite element method. The software is good at solving coupled or multiphysics problems including electrical, mechanical, fluid flow, and chemical applications. Given that in our case the Pirani pressure sensor accounts for both heat generation and conduction in the solid part and heat conduction of gas, the multiphysics solver is needed.

The Conjugate Heat Transfer module and Electric Currents module of COMSOL were the main simulating source. Two initial simulations were conducted to verify the feasibility of using the software. Fig. 3.4 shows the 2D temperature profile of a silicon beam heated under 0.4 mA current. Constant temperature boundary conditions were applied to outer chamber boundary as well as two ends of the bridge which are considered to be the anchors. The plot shows the temperature distribution within the defined cavity. For 2D simulations the software simply assume our "bridge" structure as a infinite plate, which is not the real case. Therefore, a 3D model of the bridge was then simulated with a chamber filled with air whose pressure was represented by predefined parameter, shown in Fig. 3.5. The bridge is 250 μm long, 4 μm wide and 2 μm thick. These parameters are typical for a micromachined bridge structure Pirani sensor [10]. The chamber was defined by a cavity with constant temperature boundary conditions to simulate a package kept under room
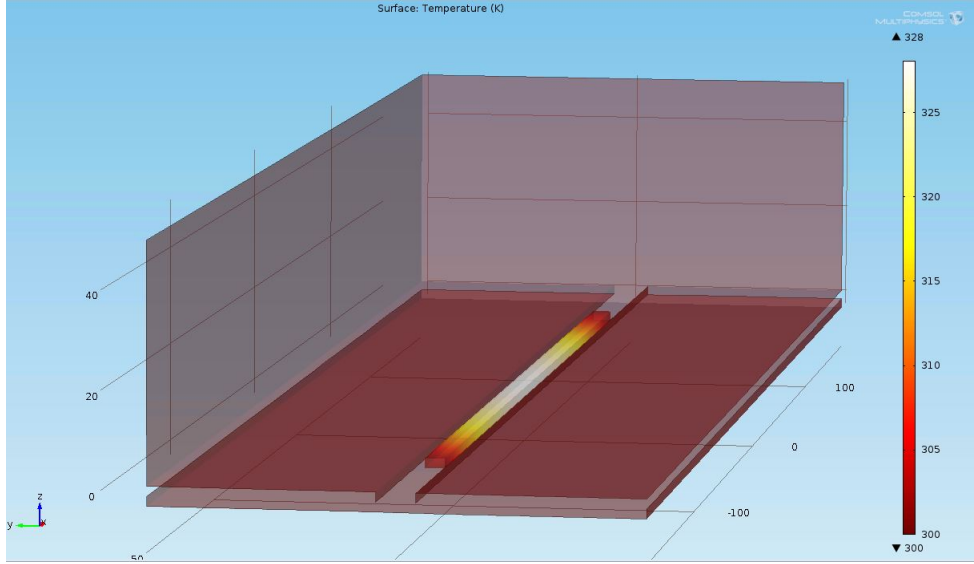
Figure 3.4: Temperature profile of 2D simulation of a single bridge structure

Figure 3.5: Schematic view of bridge design with heat sinks

Figure 3.6: Temperature profile of single bridge Pirani sensor

temperature. The domain inside the cavity was defined as fluid type "air", the pressure of which was represented by a parameter which allows the capability of doing parametric sweep to simulate the pressure change inside a sealed cavity. Note that there are two plates beside the bridge which served as heat sinks.

Fig. 3.6 shows the temperature distribution of the bridge when applying 0.5 V voltage. Note that here we tried to use constant current as we did in 2D simulation. But it turns out only using constant voltage can get our 3D simulation converge. A parametric sweep then shows the relationship between pressure change and current density in Fig. 3.7. Pressure range is from 10 Pa (75 $mTorr$) to 5000 Pa (37.5 $Torr$). The result shows the lower the pressure, the higher resistance the silicon bridge will have because of temperature rise. Based on the material properties used in the simulation, the initial resistance of the polysilicon bridge is 625 Ω. After applying the constant voltage, the resistance changed from 640 Ω to 630 Ω with respect of pressure change from 10 Pa (75 $mTorr$) to 5000 Pa (37.5 $Torr$).

After verifying the working concept of a typical Pirani sensor, a model with two large plates like "wings" with anchor attached to the centre of the bridge was built and simulated, shown in Fig. 3.8. Adding the wing structures to the bridge results in more heat sink area while maintaining the same beam resistance since no current will be flowing inside the plate structure. The parametric sweep from 10 Pa (75 $mTorr$) to atmospheric pressure shown in Fig. 3.9. It has good dynamic range from the lower limit to about 2000 Pa (15 $Torr$). It has a resistance change from 663 Ω to 636 Ω. Due to the convergence issue with current Comsol modules, simulation for lower pressure range was not possible.
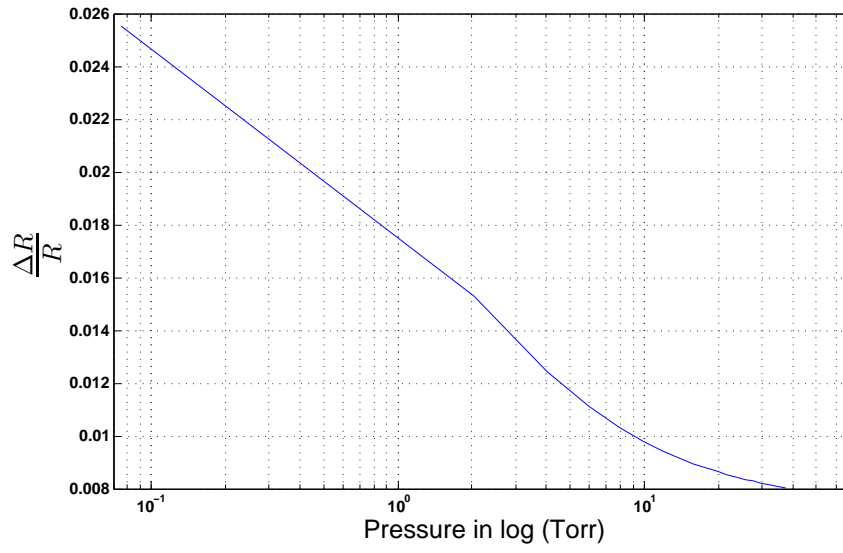
Figure 3.7: $\frac{\Delta R}{R}$ vs. pressure for single bridge Pirani sensor in simulation
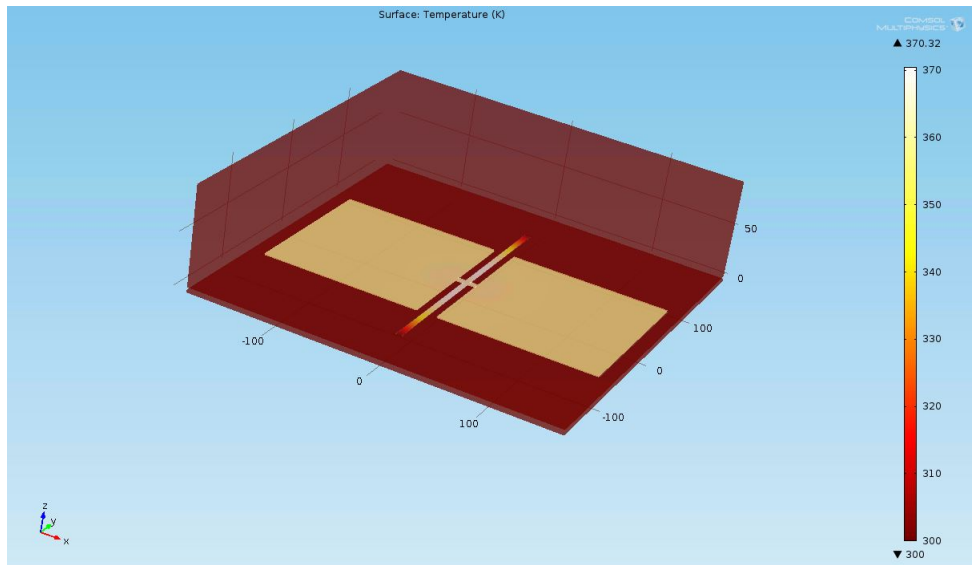

Figure 3.8: Temperature profile for "wing" structure Pirani sensor under 1 V volatege
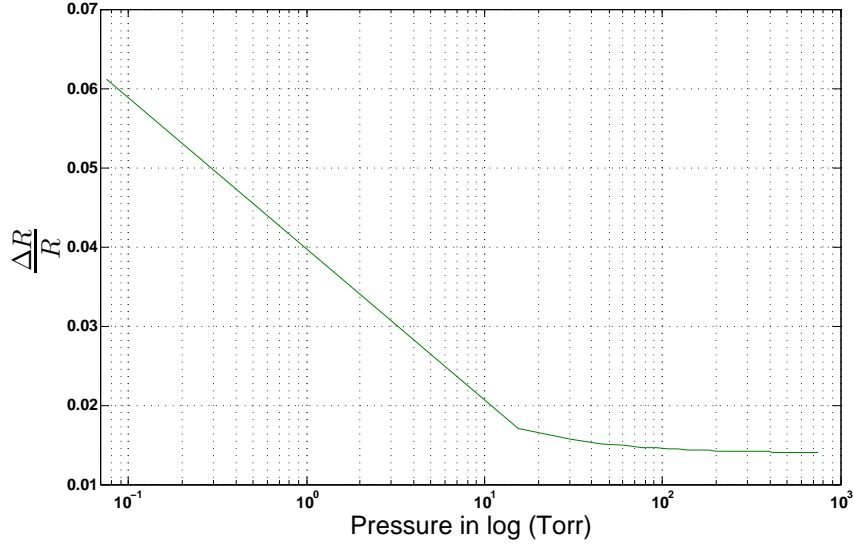
Figure 3.9: $\frac{\Delta R}{R}$ vs. pressure for "wing" structure bridge Pirani sensor in simulation

3.3 Bondwire Pirani Sensor

As discussed in Section. 3.1, when a bridge structure is heated up by current passing through it, the amount of heat dissipated to environment is a function of ambient pressure. If the "bridge" is created using a very common part inside almost every package – a bondwire, this bondwire can also serve as a Pirani sensor. Based on this hypothesis, numerical simulation and several designs of bondwire Pirani sensors were tried to test the sensor's performance and flexibility of alignment.

3.3.1 Numerical Simulation

We also developed a model in COMSOL for bondwire Pirani sensor to verify the possibility of using it as a in-package pressure monitoring element. Parameters are estimated from the size of our package as well as our gold bondwire properties. The length of the sensor is 14 mm with 25.4 μm diameter. The wire is kept inside a sealed cavity. Constant temperature boundary conditions are applied to cavity surfaces and two ends of the wire sensor, as shown in Fig. 3.10. A 0.07 V voltage is applied to generate heat along the sensor.

Based on this model a parametric sweep for pressure is conducted from 10 Pa (75 $mTorr$) to 10^5 Pa (750 $Torr$). Fig. 3.11 shows the $\frac{\Delta R}{R}$ vs. pressure curve, which accords with the "S" curve mentioned in Section. 3.1.2. Result shows a dynamic range with upper bound to be around 50 $Torr$. This proves the concept of using bondwire as an in-package Pirani sensor. Notice that due to convergence issue, the lowest pressure that could be achieved
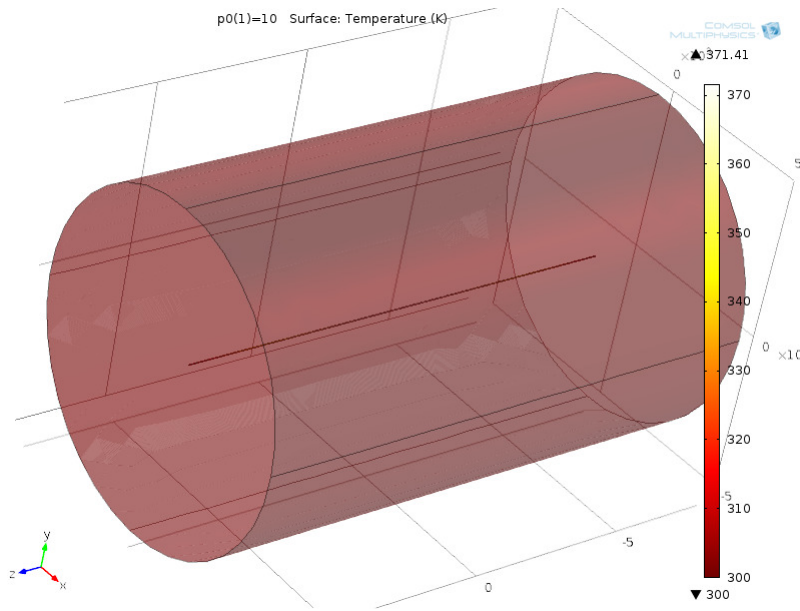
28

Figure 3.10: Temperature profile of bondwire Pirani sensor simulation at 10 Pa (75 $mTorr$) pressure
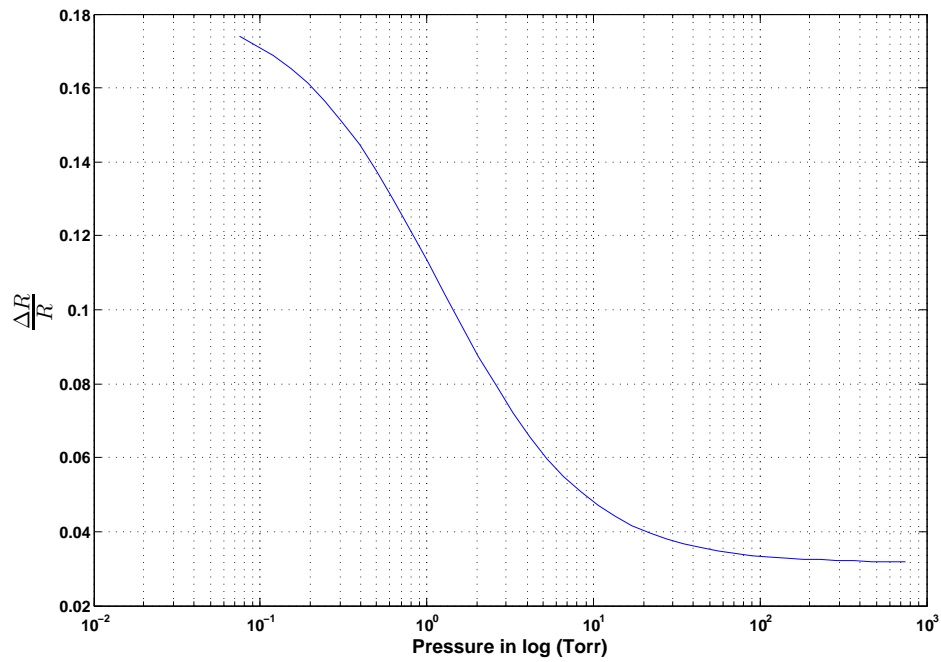

Figure 3.11: $\frac{\Delta R}{R}$ vs. pressure for bondwire Pirani sensor in simulation
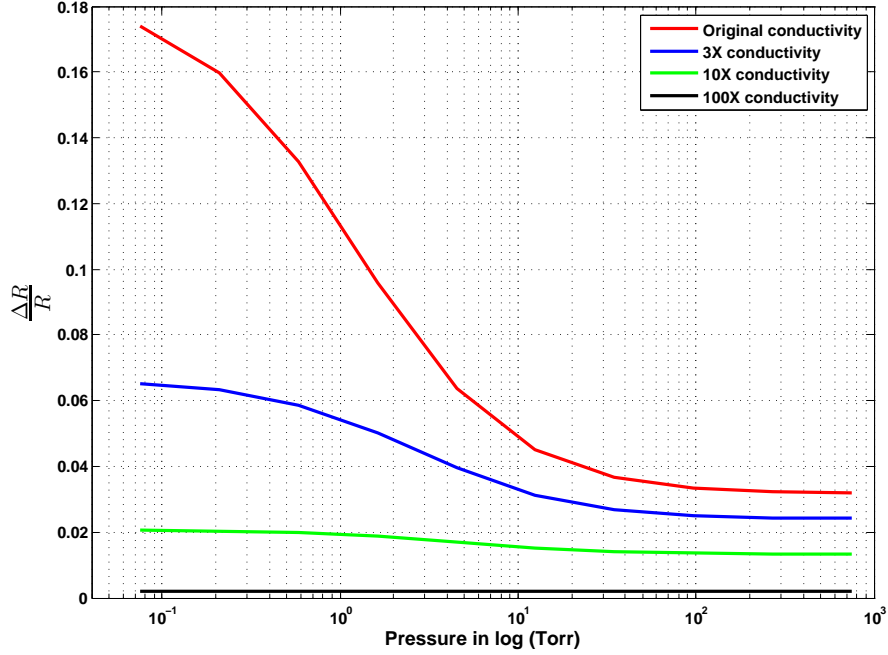
Figure 3.12: Response curves combined with different gold conductivity

was 10 Pa (75 $mTorr$). At the lower pressure range the response curve is showing a trend of saturation as a result of low gas thermal conduction which makes heat conduction by solid anchor parts dominant the heat dissipation process. More sets of simulation were done to further verify this concept and to make the lower pressure range saturation more clear without the capability of going into the pressure lower than 10 Pa (75 $mTorr$).

By simply changing the conductivity of the solid part (Gold wire), the portion of heat loss through the anchors were artificially increased which would in turn shift the lower bound of saturation of the response curve to the right. A few simulations were done based on this hypothesis. Fig. 3.12 indicates that the response curve had a significant rightward shift as conductivity of gold increasing. Meanwhile, as heat conduction by solid part was increased, the sensitivity of sensor decreased dramatically. That also enlightened us that in order to have a good Pirani sensor the ratio of heat dissipated by gas over solid parts should be minimized.

However, using bondwire as Pirani sensor has several challenges that need to be resolved. Otherwise, data collected by the sensor cannot be effectively used.

- To ensure that our sensor is low cost and does not demand extra work, using a
  regular wirebonding machine is the preferable way. In general, there are two kinds of

30

Table 3.1: Resistance distribution of every part of measurement set up

Part Name	Resistance(unit Ω)
Bondwire sensor	0.659
Contact resistance	0.006
Package	0.275
Cable	1-2

wirebonding techniques namely ball bonding and wedge bonding. Also two types of materials are prevalently used: Aluminium and Gold. The resistance of such gold or Al wires inside a typical ceramic package is usually in 0.1 Ω range. The mechanism of a Pirani sensor is based on detecting the resistance change of a bridge. Measuring resistance change of such small resistor is challenging.

• Four-point measurement is often the preferred solution for measuring low resistances. By passing current through the resistor with two probes and measure the voltage difference, a much more accurate result is obtained. This kind of four point measurement often needs the help of probe stations to give the electrical source proper access to small structures inside package cavity [35]. Only by doing so can we get rid of the series resistances of the package, the contact resistance of the bonding point, etc. However, it is obvious that using four-point probe measurement set up is too complicated for our case since the bondwire Pirani sensor should be applicable for measuring the pressure change inside a sealed cavity, in which case there is no direct access to the anchors of the bondwire sensor.

• The bondwire is very sensitive to the environment change which may be included along the whole packaging procedure. That makes getting the correct characterization curve more difficult.

3.3.2 In-package Four Point Measurement Setup

In this section, our basic set up of bondwire sensor is firstly described which makes four-point measurement from outside the package possible. Then the full characterization process is presented, along with the way to build experimental environment. Results are discussed to justify that our bondwire sensor is capable of monitoring the desired pressure range. Several tests are done to show the repeatability of bondwire sensor. Long-term pressure measurement is demonstrated at last to show the stability of the bondwire sensor.

First of all, Table 3.1 shows the resistance distribution when taking regular measurement from outside the package. Measurements were taken with Janis ST-500 probe station. To verify this result, one might consider the properties of the goldwire as shown in Table. 3.2. Length of the sensor is calculated with regular properties of gold, which accords with our

Table 3.2: Physical properties of gold wire sensor

Property	Gold	Aluminium
Resistivity	$2.249 \times 10^{-6} \ \Omega \cdot cm$	$2.65 \times 10^{-6} \ \Omega \cdot cm$
TCR	$3670 \ ppm/^{\circ}C$	$4290 \ ppm/^{\circ}C$
Diameter	$1mil$ $(25.4 \ \mu m)$	-
Length	about $1.4cm$	-

sensor length. Note that solely package resistance is at the same order of magnitude as sensor resistance. This test is taken with LCC package, which has very low package body resistance. If other kind of package is required for example Side-Brazed Dual In-Line Ceramic Package (SBDIP) or Leaded Chip Carrier (LDCC), this value may be even greater. By following the regular measurement steps it is impossible to get useful data since SNR (signal noise rate) becomes too large.

In general, the best solution for such scenarios will be four point measurement. A four point measurement, or four-terminal sensing, is designed for accurate impedance measurement. By supplying current through the target impedance with two source terminals and point the other two sense terminals immediately adjacent to the target impedance to measure voltage drop, the measurement reading now does not include the voltage drop of any resistor in series like the force leads or contacts.

Bonding pads
inside package

Sensor bondwire

Connection
bondwire

Voltage
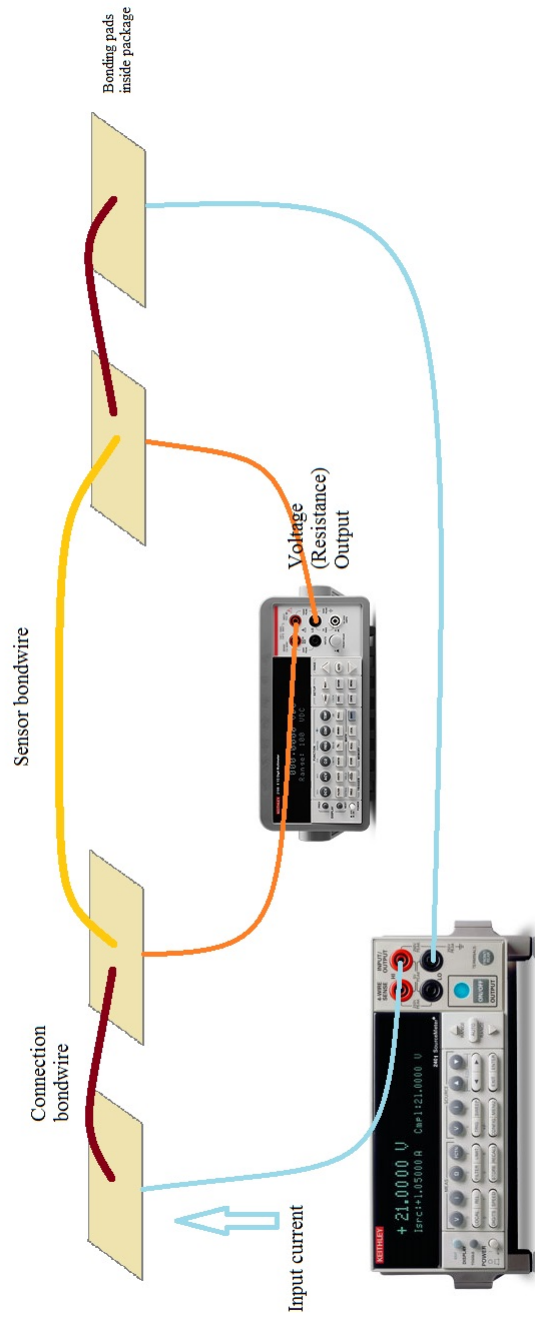(Resistance)
Output

Input current

Figure 3.13: Bondwire sensor with double-side connection.

Therefore, our main thinking is to be able to complete four-point measurement from outside the package. So that once the package is vacuum sealed, it is still possible to get useful data out of it and know the exact pressure inside. Our answer to this question is simple but effective: we created two short bondwires and connect them to each end of the sensor bondwire. As shown in Fig. 3.13. That created access from outside the package to both ends of the sensor. By sending current from the outer two connection pads and measuring the voltage drop from inner ports, four-point measurement is achieved without any extra cost. Since Table. 3.1 indicates that contact resistance is almost negligible (it was a gold to gold welding), this measurement set up can give us satisfactory results.

The bondwire sensors are put into Janis Vacuum Test Chamber for characterization. The chamber is capable of regulated pressure from 6 $mTorr$ to 760 $Torr$. The digital pressure display unit of the chamber has a calibrated vacuum gauge from Kurt J. Lesker. One good thing about this pressure unit is that it provides RS-232 port for data acquisition, which enables automatic Labview aided data writing and figure plotting.

Chapter 4

Hermetic Packaging Process

As discussed in Chapter 2, CLP is the proper packaging technique for research based MEMS devices. It can tolerate a wide scale of device variety including dimensional change, material change or even fabrication flow change. In this chapter, the whole hermetic packaging process developed for MEMS devices is reported. The packaging system is briefly introduced, followed by the detail packaging process flow.

4.1 The SRO-700 Vacuum Packaging System

The packaging system is an ATV solder reflow oven (SRO) with IR heating, shown in Fig. 4.1. It is capable of doing die attachment, vacuum encapsulation or even wafer level packaging and is ideal for R&D process development. Some of the key features of the system include:

- Operating maximum temperature: $450°C$, up to $750°C$

- Heating area: 230×217 mm

- Fast heat ramping

  - Ramping up $> 3.5°C/second$
  - Ramping down $> 2°C/second$

- Rapid single wafer processing $> 20°C/second$

- 100 steps per program

- Oxygen $< 1.0\ ppm$

- Formic acid activated nitrogen

Figure 4.1: Photograph of SRO-700 packaging system

- Ultimate vacuum $5 \times 10^{-5}\ mbar$

The system needs several source supplies to ensure its functionality:

- cooling tap water 2.5 l/min: for cooling down the heating chamber.

- dry nitrogen $3 - 6\ bar$: for cleaning as well as cooling the chamber.

- compressed air $5 - 7\ bar$: controlling the valves actuation.

- ventilation treatment: needed if formic acid vapors used.

4.2   Packaging Process Development

Although MEMS packaging differs from device to device, a standard MEMS CLP process mainly contains the following three steps [43]:

- Die attachment: to attach device chip solidly to the chip carrier to ensure the mechanical support and avoid vibration.

- Wire bonding: to create electrical connection between device and chip carrier so that there is electrical access from outside the package.
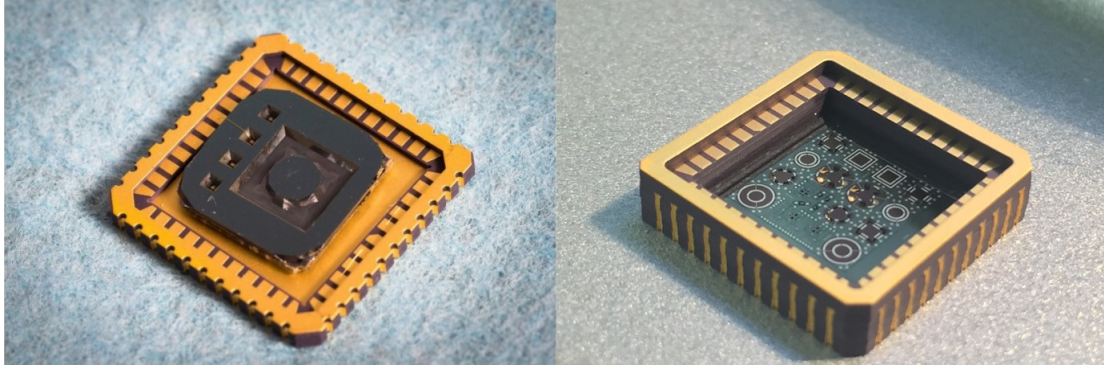
Figure 4.2: Picture of our LCC packages: shallow one to the left and deep cavity one to the right

- Encapsulation: to hermetically seal the package in order to have a stable internal environment.

Our project aims to have a reliable hermetic packaging process that is repeatable and has a robust seal. In this section, the packaging process design is described step by step with material choice for each step.

4.2.1 Die attachment

First of all, as discussed in Section. 1.2, 44 pin LCC package was chosen as our chip carrier. The ceramic chip has the advantage over others not only in size, but also enables accurate sensing with its high modulus of elasticity and flexural strength. It can also save us from using thermal vias or heat spreaders because of its high thermal conductivity and low CTE [43].

Two kinds of 44 pin LCC packages with different cavity depths are available to serve different thickness devices. As shown in Fig. 4.2, inside the package is coated with 99.9% pure gold over nickel. The seal ring part on package is electrically isolated. Area of cavity is $12.04(\pm0.25) \times 12.04(\pm0.25)$ mm^2 and depth is $0.5(\pm0.05)$ mm and $2.24(\pm0.23)$ mm respectively.

Presently, solders, adhesives and epoxies are commonly used for MEMS die attachment. The device chip, die attach material and chip carrier form a sandwich structure as shown in Fig. 4.3. The main distinction between solders and adhesives/epoxies is the operating temperature. Generally, adhesives and epoxies comprise a bonding material filled with metal flakes which may require a curing temperature between $100°C$ and $200°C$. However, for MEMS inertial sensors, Q factor is a crucial parameter to the device operation. Unfortu-
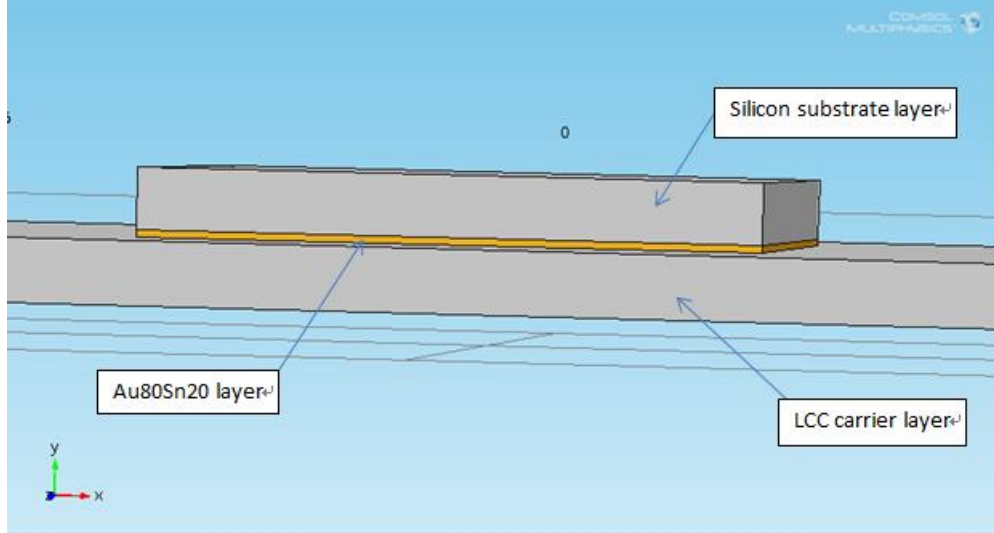
Figure 4.3: Schematic view of die attachment for MEMS

nately, epoxies and adhesives may cause Q factor instability and aging issues as a result of outgassing and humidity increase.

Therefore, Au80/Sn20 alloy was chosen as our die attachment material. The alloy is from Indium Corporation of America and comes in square preform (Fig. 4.4) with 6.32 mm length of each side and 0.025 mm thickness. That gave us the flexibility of doing the die attachment for a wide variety of devices. Given the LCC package is already bottom Au plated, the device die would need a backside gold coating in order to use solder die attachment material, shown in Fig. 4.5.

With correct assembly shown in Fig. 4.3, the whole package was heated up to a temperature slightly higher than the eutectic Au/Sn melting point (about $300°C$) for a short time. Then the rigid die attachment was formed. The whole die attachment process is done in our SRO-700 system.

4.2.2 Wire Bonding

An electrical connection between device and chip carrier needs to be created, shown in Fig. 4.6. With the help of K&S 4700 Wire Bonder at Simon Fraser University 4DLabs [44], standard 1 mil Au wire was used for this work. Different bonding strategy might be applied to different devices.

After wire bonding step, the package is ready for testing and characterization if needed. It will be temporarily covered by a transparent lid to prevent dust and other contaminations. A P2044S-BAU open-top socket, as shown in Fig. 4.7, can help with the testing.
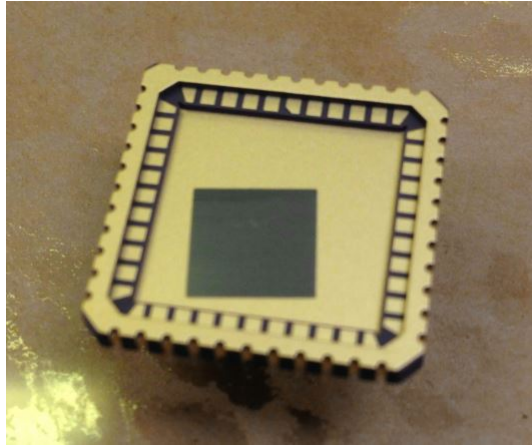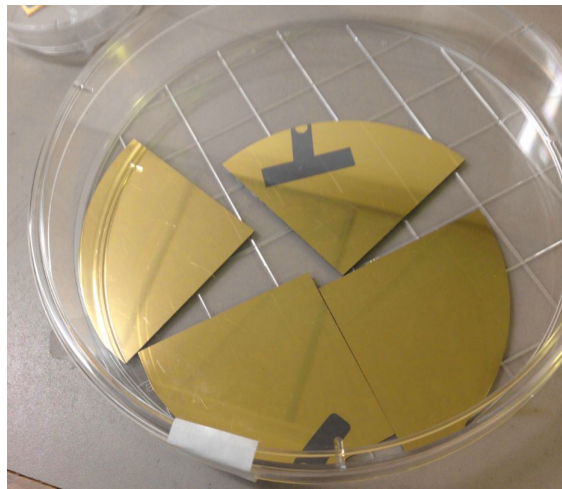
Figure 4.4: Photo of Au/Sn preform

Figure 4.5: Photo of device die backside Au PVD as die attachment prerequisite
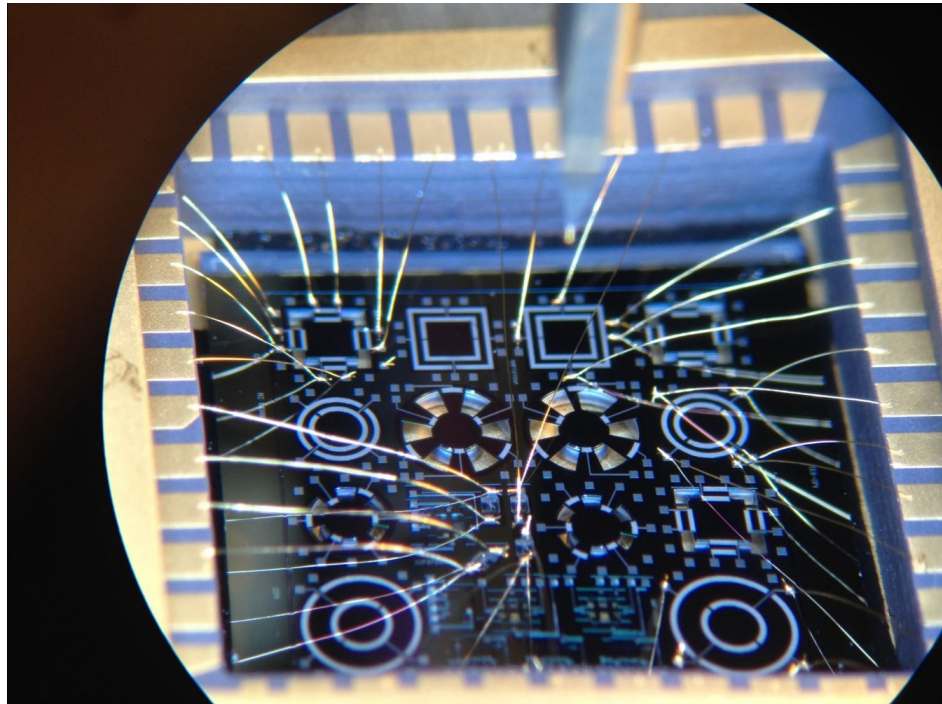
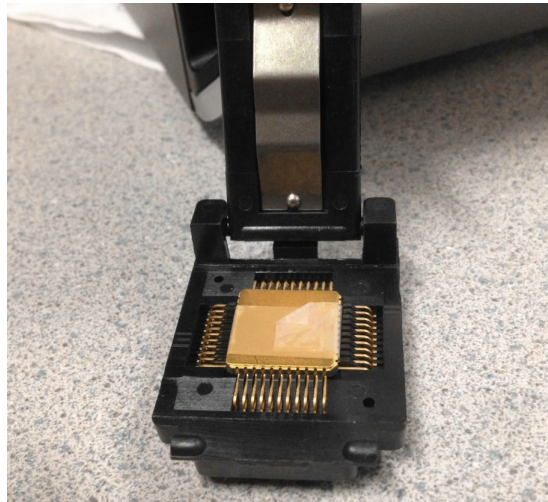Figure 4.6: Photo of Au wire welded devices by wedge bonder

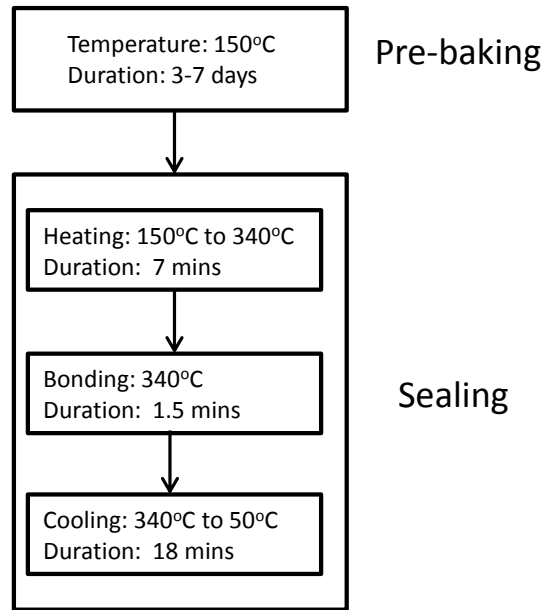Figure 4.7: Photo of testing socket for LCC44 package

Figure 4.8: Regular encapsulation process flow)

4.2.3 Encapsulation

Apparently this is the most critical step throughout the whole packaging process. The quality of seal directly determines the internal environment. The entire process flow was conducted inside our vacuum packaging system, shown in Fig. 4.8.

When choosing package and die attachment material, close attention was addressed to outgassing and hermeticity issue. On top of that, a thoroughly baking before sealing is essential as described in Section. 2.1. By doing so the residual gas or moisture trapped inside package cavity or on surface of devices can be wiped out. The baking is suggested to last at least 3 days under a pressure of 0.1 Pa (0.75 $mTorr$) and 150°C temperature [45].
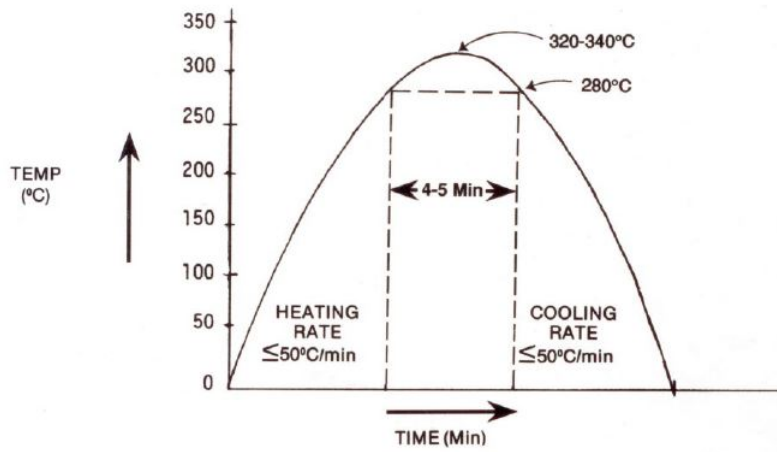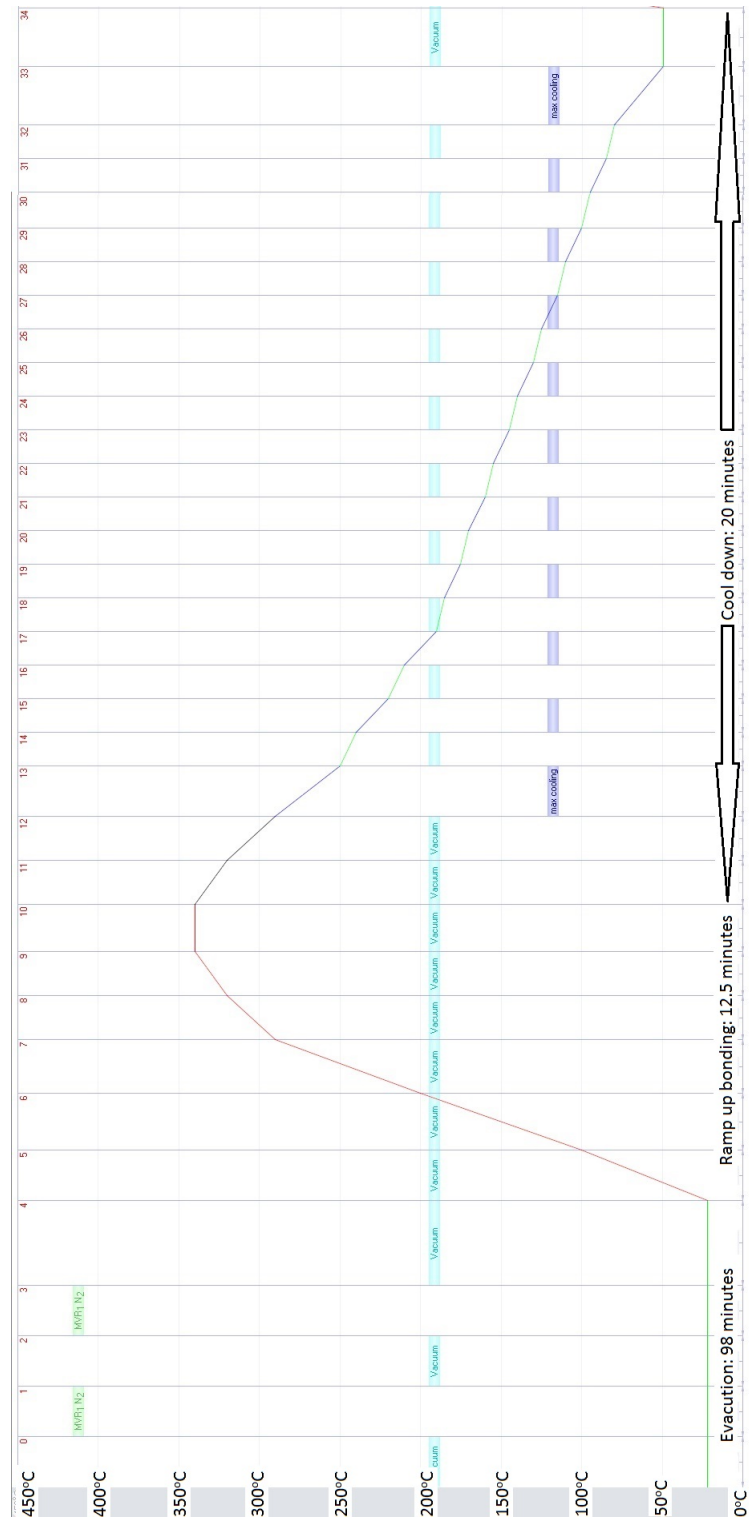
Figure 4.9: Suggested sealing profile

Figure 4.10: Sealing program in ATV file format

Figure 4.11: Photo of weight on package when sealing

A combo lid made of Kovar alloy with Nickel and pure Gold plated was chosen as the package cover. It also has a preform solder ring along the edge. A sealing process based on vendor recommendation was developed that resulted in a reliable encapsulation (Fig. 4.9). The sealing step program is shown in Fig. 4.10: a nitrogen/vacuum cycle at the very beginning to clean up; then the package was heated up under vacuum to around $340°C$ to complete the eutectic bonding; then the whole chamber was cooled down using nitrogen/vacuum cycle. When sealing, a weight is also put on package to ensure correct alignment of the lid (Fig. 4.11). The weight is designed to be having least contact area to avoid heat loss when forming eutectic bond.
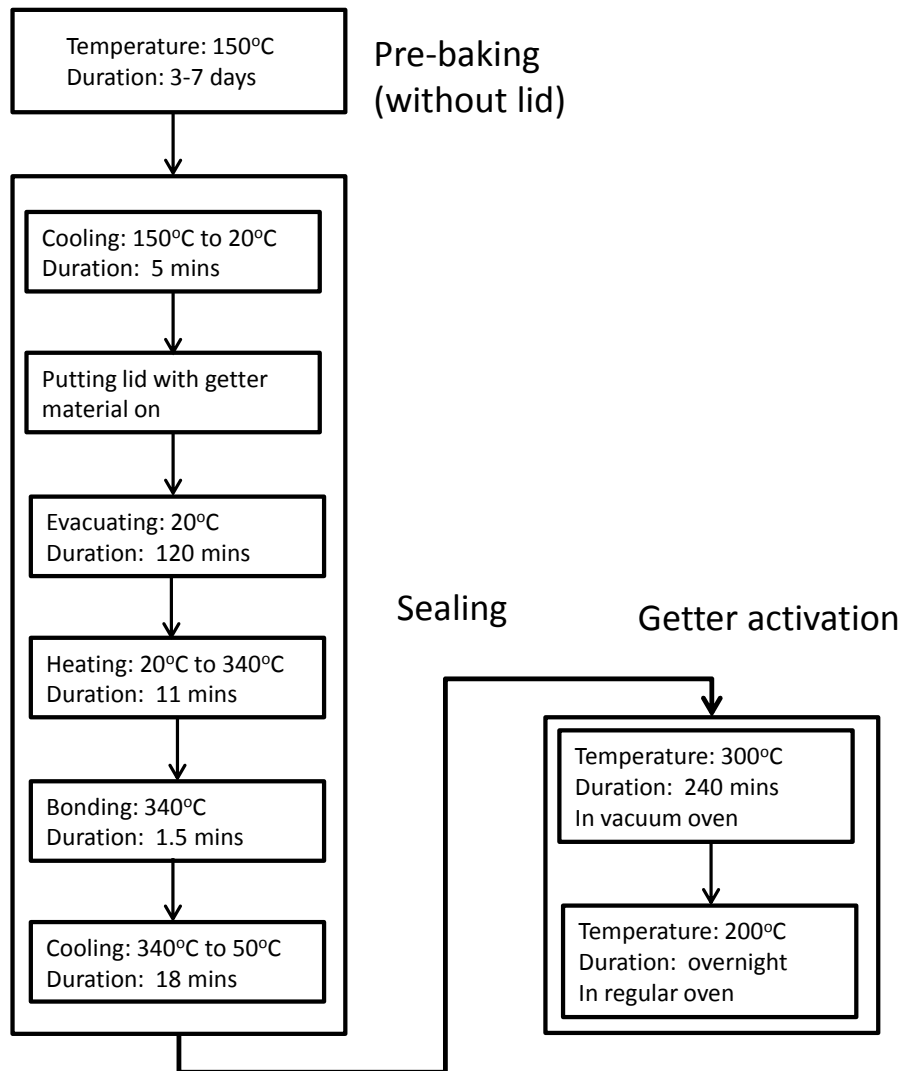
Figure 4.12: Encapsulation with getter activation (getter material deposited on combo lid)
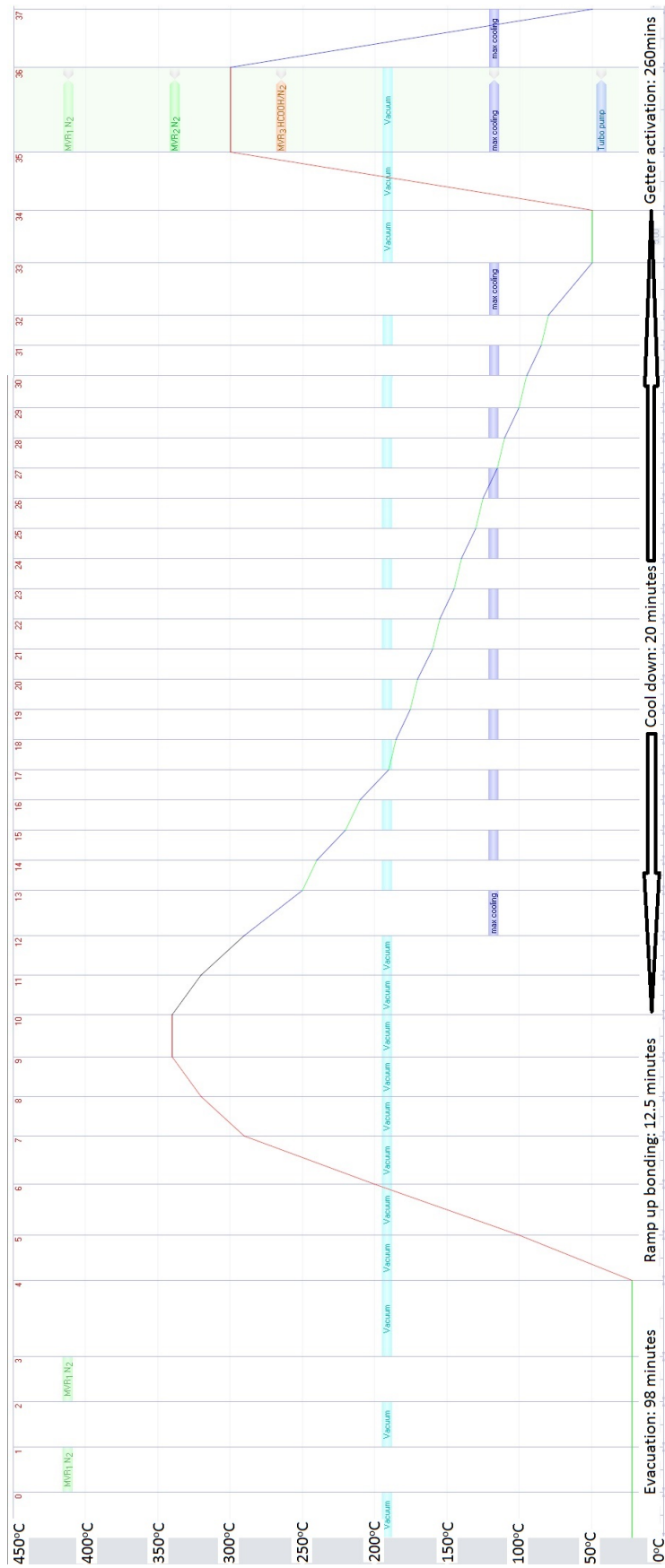
Figure 4.13: Sealing program for getter involved applications

The ultimate pressure that can be achieved with this packaging procedure is believed around 1.5 $Torr$ limited by outgassing. To push the lower limit of packaging pressure, one could consider using getter material. We deposited a getter material on some of the lids through a commercial provider. Heating the lid with getter material prior to the sealing step is prohibited because that will cause premature getter activation. A detailed process flow with getter involved encapsulation is shown in Fig. 4.12. The differences between this one and the regular process are:

- In a regular encapsulation process, the lid and package are kept inside the vacuum system at the very beginning from "pre-baking" step. Since getter material is extremely sensitive to thermal treatments, the lid with getter deposited can only be put into the vacuum system between pre-baking and sealing to avoid improper activation. The vacuum system will be cooled down and opened in order to put lids on package for sealing alignment. Then the whole system will be evacuated once again before applying the sealing temperature profile.

- After sealing the package, a getter activation step is added to make the getter material fully functional. This step contains two parts: a 4-hour $300°C$ vacuum baking (main activation) and an overnight $200°C$ regular baking (post-activation). The post-activation has been proved to be effective in terms of thoroughly activate the getter material.

From current packaging runs, the sealed pressure was improved to 0.3 $Torr$ with getter material in package. The packaging process program based on getter involved sealing is shown in Fig. 4.13.

Chapter 5

Experimental results

In this chapter, test results of our devices are presented. Bondwire Pirani sensors with different layouts were tested and characterized inside our LCC packages. The packages were then sealed and tested to justify the packaging process's reliability. Longterm monitoring was also conducted on bondwire sensor. The practicability of utilizing bondwire sensor was verified. Silicon micromachined devices were tested as well. However, due to its disadvantage in compatibility over different device process flow, we implemented the bondwire sensor as our prevalent solution.

5.1 Test setup detail

Basic test setup for characterizing pressure sensors includes the Janis Vacuum Chamber for regulating pressure values and a Keithley 2400 source meter for taking measurements. As shown in Fig. 5.1 the chamber is equipped with a reference pressure sensor with display. Pressure can be controlled by a vacuum pump and several valves with different fineness. The packages were put inside this chamber with electrical connection created through sealed feedthroughs. A Labview program was developed to read and write data from sourcemeter and Lesker pressure gauge to a file. The program is also capable of displaying the data in real time. The complete characterization setup is shown in Fig. 5.2.

After the encapsulation step, the sealed package was tested for long periods. Setup for this test is helped by our NI-PXIe PC-based testing platform (Fig. 5.3). The package was kept isolated with a thermocouple sensor side by side to see the relationship between room temperature variations and output signal fluctuations. Complete setup shown in Fig. 5.4.
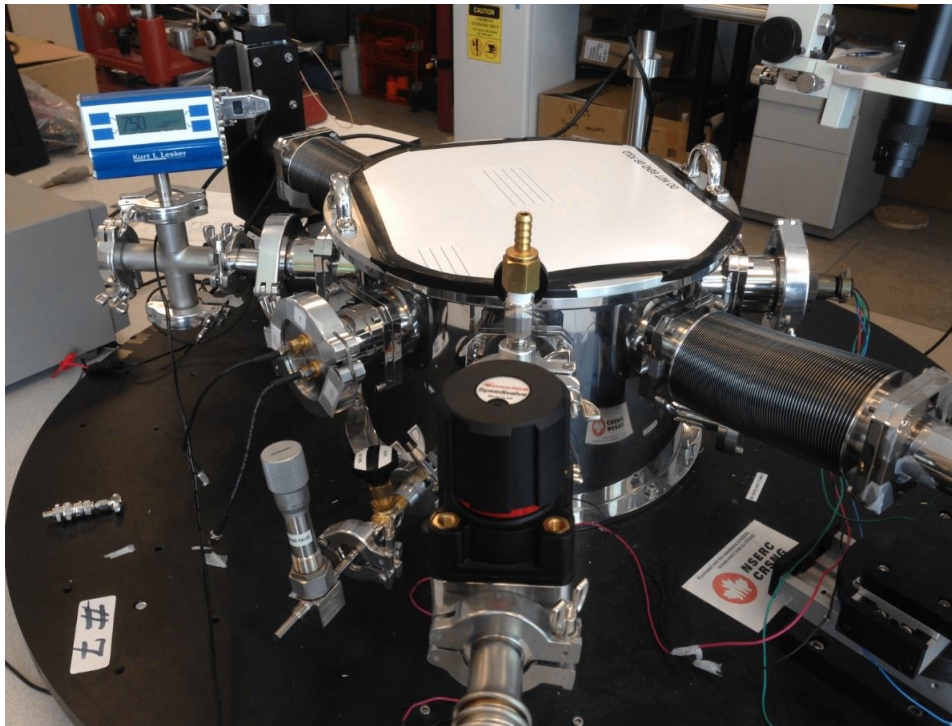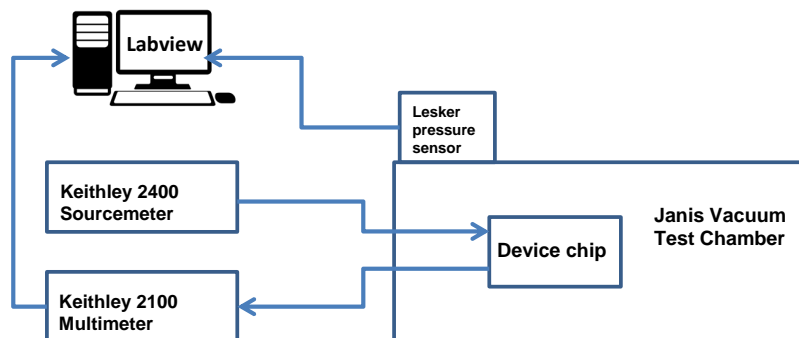
Figure 5.1: Picture of Janis Vacuum Chamber

Figure 5.2: Setup for Pirani pressure sensor characterization

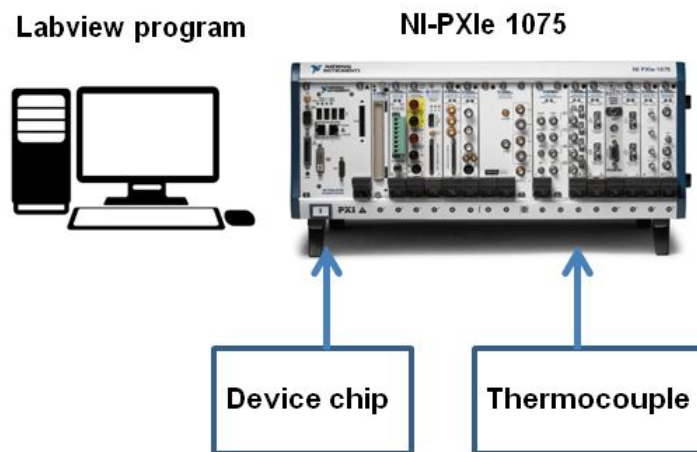Figure 5.3: NI-PXIe testing platform

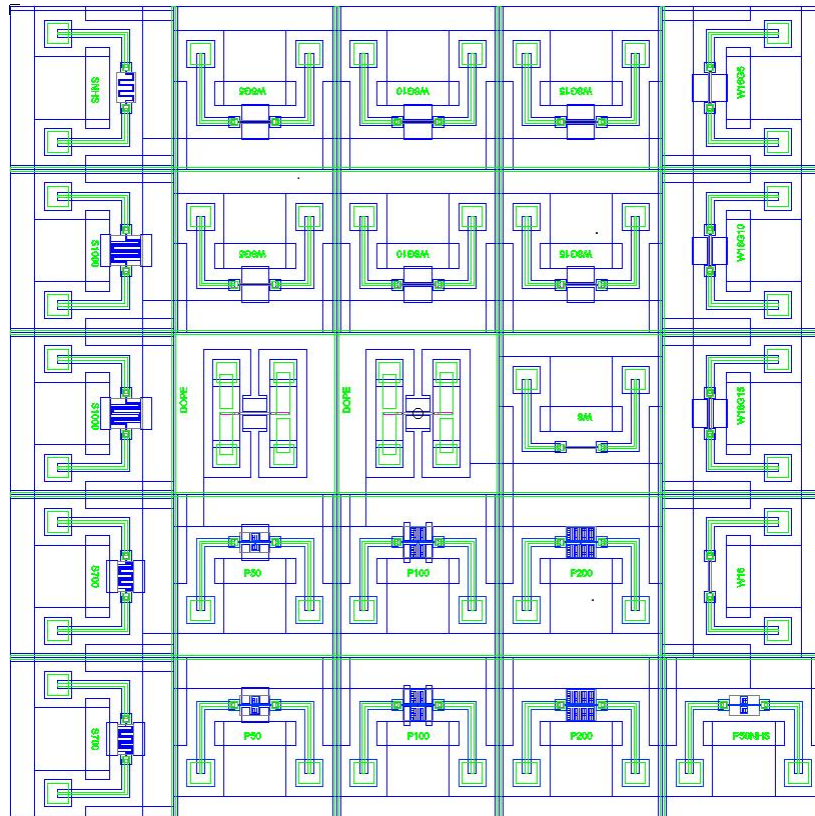Figure 5.4: Setup for longterm testing of bondwire Pirani sensor

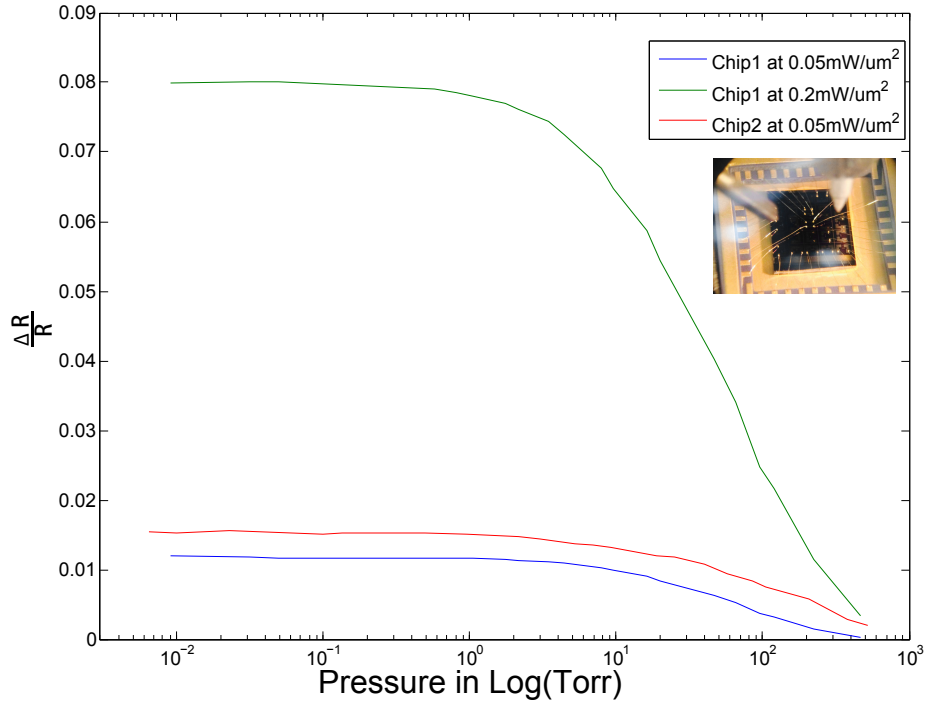Figure 5.5: Design layout for silicon Pirani sensors

Figure 5.6: $\frac{\Delta R}{R}$ vs. pressure curve for two silicon micromachined Pirani designs

5.2 Experiment results

5.2.1 Silicon Pirani Sensor

The microfabricated dies were fabricated by my colleague, Amin Rasouli, SOI process design shown in Appendix A. Design layouts shown in Fig. 5.5. Detailed information about design labelling is provided in Appendix B.

Due to the low doping process of our previous micromachining, most of the sensors could not work as Pirani sensor because of their high resistance (in $M\Omega$ range). Three different chips were tested and some data was obtained from "DOPE" devices. From Fig. 5.6 it can be seen that dynamic range of our sensor is from $1\ Torr$ to atmospheric. For the same chip, the higher power density used, the better sensitivity can be expected.

Refer to Section. 3.2.2, the resistance of a bridge Pirani design with the same length is 625 Ω while the measured resistance for our fabricated device is about 500 Ω. The normalized outputs $\frac{\Delta R}{R}$ change from 0.02 to 0.06 in simulation and 0.01 to 0.08 in experiment under the same 0.2 $mW/\mu m^2$ power density. Hence, our simulation predicted the experimental result.
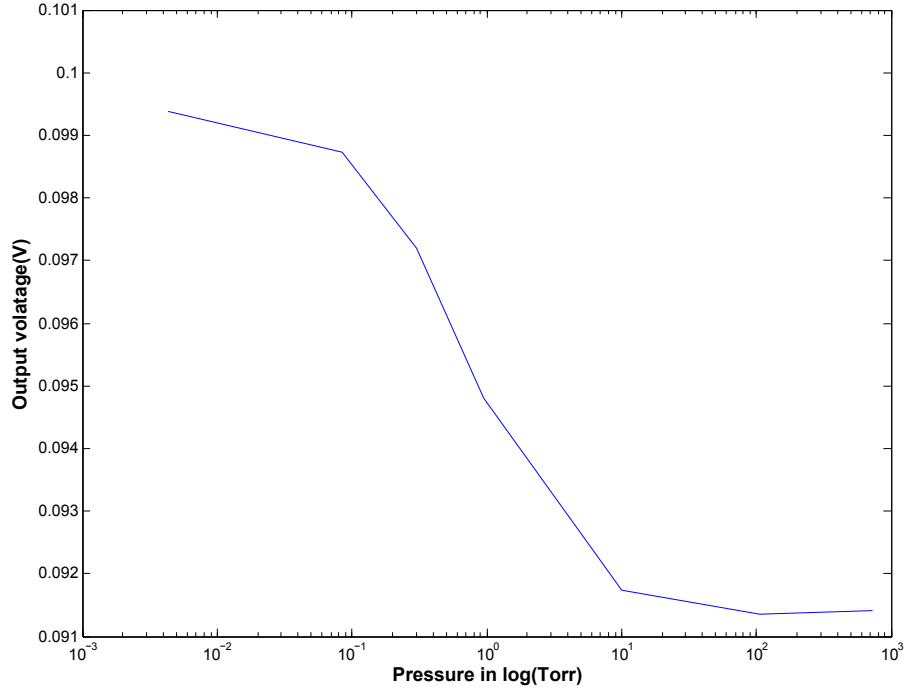
Figure 5.7: Voltage vs. pressure curve for a trial bondwire sensor under 100mA current

5.2.2 Bondwire Pirani Sensor

After some simple tests for bondwire sensor, the feasibility of using it as Pirani sensor was verified, shown in Fig. 5.7. The figure shows that the sensor saturates at both ends but lower bound of dynamic range is better than the silicon design.

More bondwire sensors were then fabricated and characterized based on the aforementioned four point measurement to achieve accurate measurements, as shown in Fig. 5.8, 5.9, and 5.10. We tried to verify the feasibility of different bondwire sensor alignment to allow us flexibility of applying this technology to different devices. Detail bonding map for bondwire sensors are described as follows:

- Chip "LABC" contains 3 long bondwire sensors across the package body. Resistance of each wire is around 0.6-0.7 Ω, shown in Fig. 5.8.

- Chip "EDGE" contains 6 bondwire sensors across the edges of package. The short wires without labels are the connection wires for four point measurement (see Section. 3.3.2), shown in Fig. 5.9. Individual device label shown in the figure.
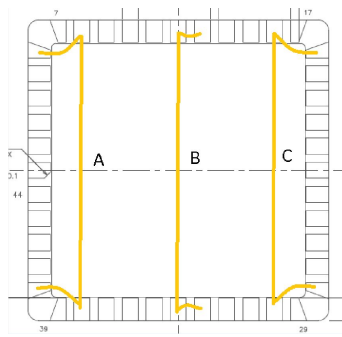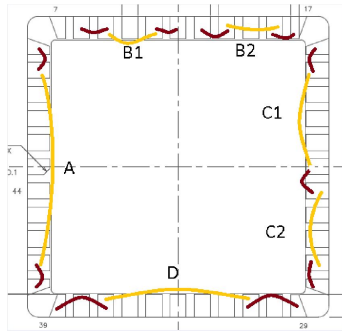
Figure 5.8: Bonding map for chip LABC
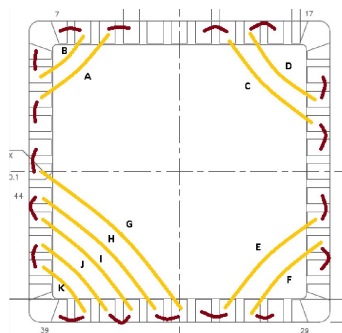

Figure 5.9: Bonding map for chip EDGE

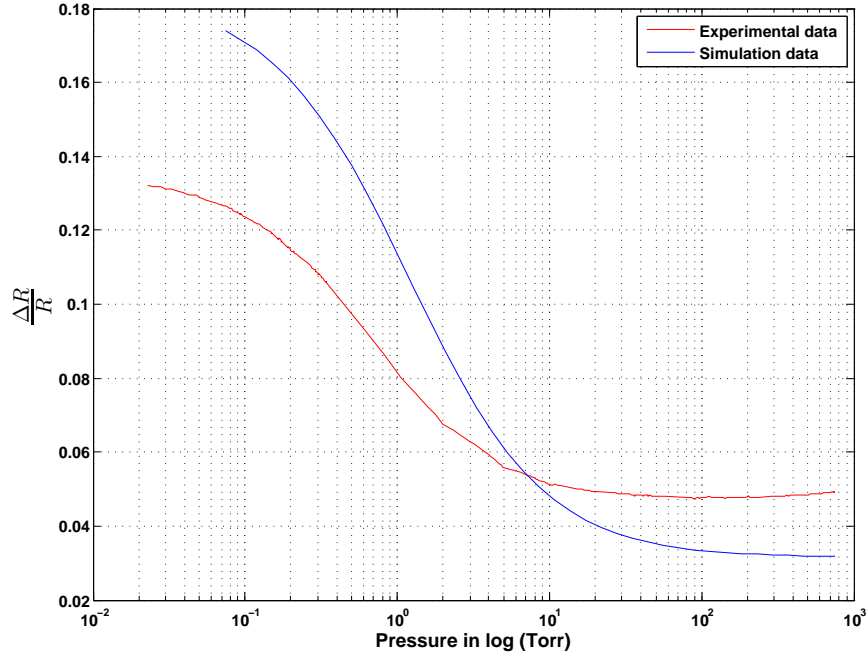Figure 5.10: Bonding map for chip CORNER

Figure 5.11: $\frac{\Delta R}{R}$ vs. pressure comparison between simulation and experiment

• Chip "CORNER" contains 11 bondwire sensors across the corners of package. The short wires without labels are the connection wires for four point measurement (see Section. 3.3.2), shown in Fig. 5.10. Individual device label shown in the figure.

LABC chip was firstly tested. Data from device A was then compared with that in COMSOL simulation. The dimension of device A is about the same as the simulation model. Power density were chosen as around the same level. Fig. 5.11 shows the comparison of two outputs. They basically follow an "S" curve as expected. The simulation result also predicted dynamic range of the bondwire sensor very well. Note that the lower bound of our simulation was confined around $10\ Pa\ (75\ mTorr)$ due to convergence issue.

Fig. 5.12 shows the characterization curve for device A, B and C under 50mA current. Different current tests were also done on single device to show the relation between current density and sensitivity of the sensor. In Fig. 5.13, four curves show the response under different currents. As the same in the silicon sensor case, the higher power density leads to better sensitivity. Repeatability was also tested for all devices, data shows that the readings were close to each other in their dynamic range (Fig. 5.14).

Fig. 5.15 shows the characterization data for chip EDGE. Different ways of welding the sensor wire were tried and their feasibilities of being used as Pirani sensor were verified.
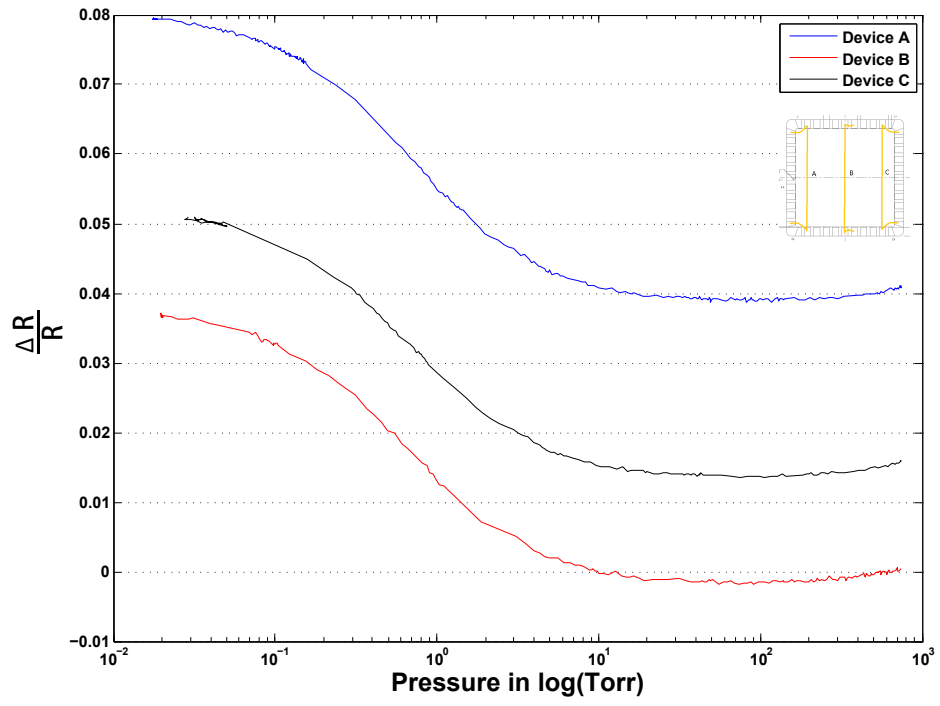
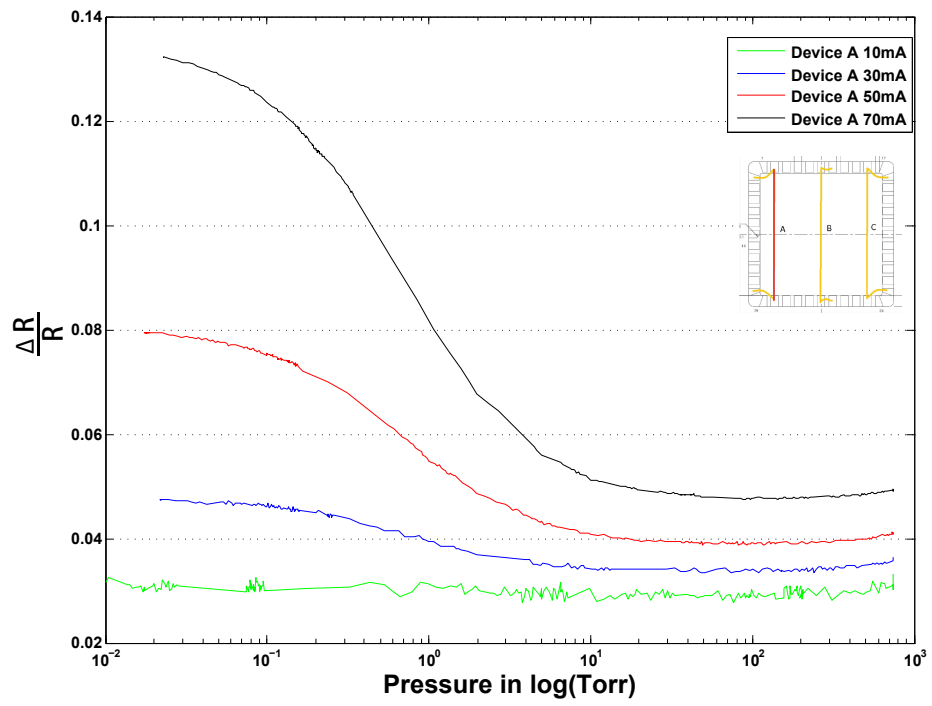Figure 5.12: $\frac{\Delta R}{R}$ vs. pressure curve for chip LABC under 50mA current

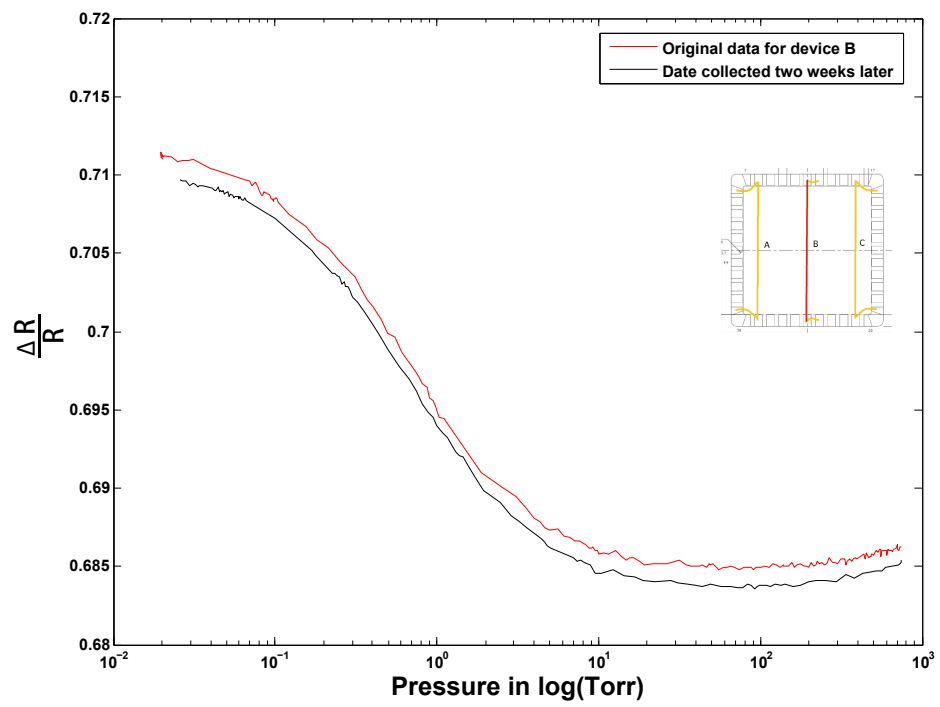Figure 5.13: $\frac{\Delta R}{R}$ vs. pressure curve for chip LABC device A with different currents

Figure 5.14: $\frac{\Delta R}{R}$ vs. pressure curve repeatability measurement for chip LABC device B
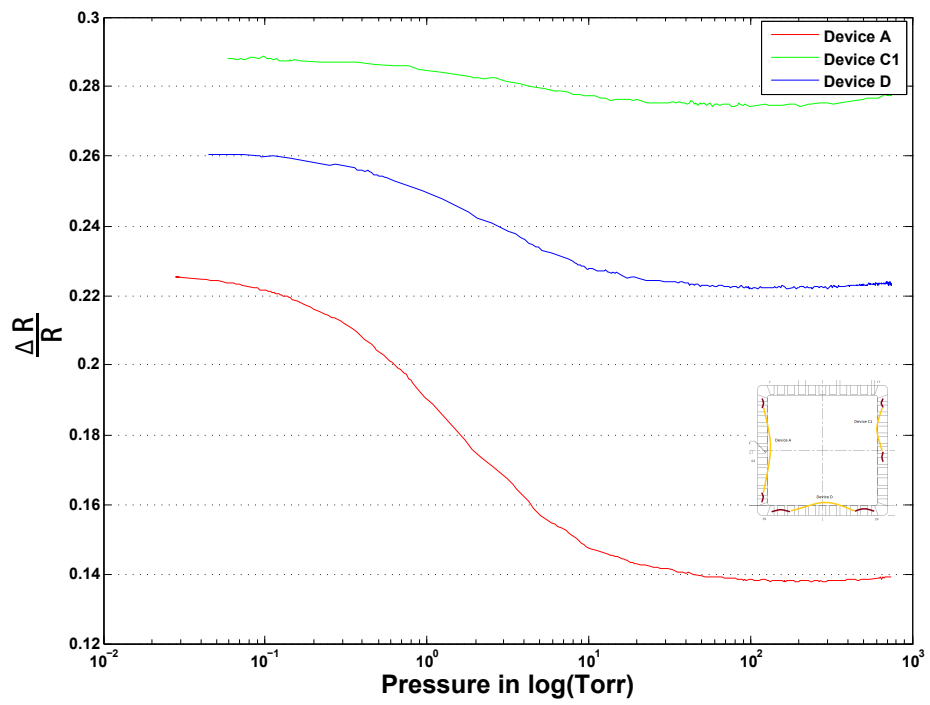
Figure 5.15: $\frac{\Delta R}{R}$ vs. pressure curve for chip EDGE under 100mA current
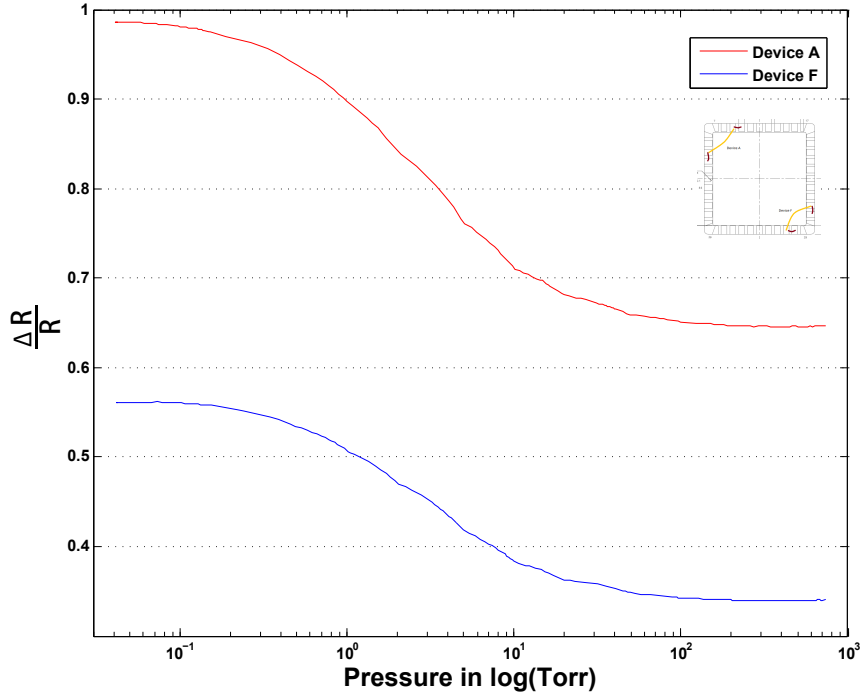
Figure 5.16: $\frac{\Delta R}{R}$ vs. pressure curve for chip CORNER device A, C, F under 400mA current

For device B1, B2 and C2, since the sensing wire is too short, no meaningful data could be obtained. That accords with the conclusion in Section. 3.2.1.

Data for chip CORNER is shown in Fig. 5.16 and Fig. 5.17. Device A and F have pretty much the same response due to their same length. And device C seems to have a better performance. For device JG and KG, current was applied across this serpentine bonding structure. That gave us multiple choice of how to test different length wires. An interesting find is that, as shown in Fig. 5.17, add short wire K to the whole heating part is adversely affecting sensor's performance.

By far, the possibility and feasibility of using a bondwire Pirani gauge inside an off-the-shelf LCC package was thoroughly illustrated.

5.2.3 Encapsulation pressure analysis

In our project, the core application of the Pirani sensor is to monitor the pressure change inside a sealed package for our MEMS accelerometer devices. Therefore it is important to prove that the bondwire sensor can sense the pressure after sealing.
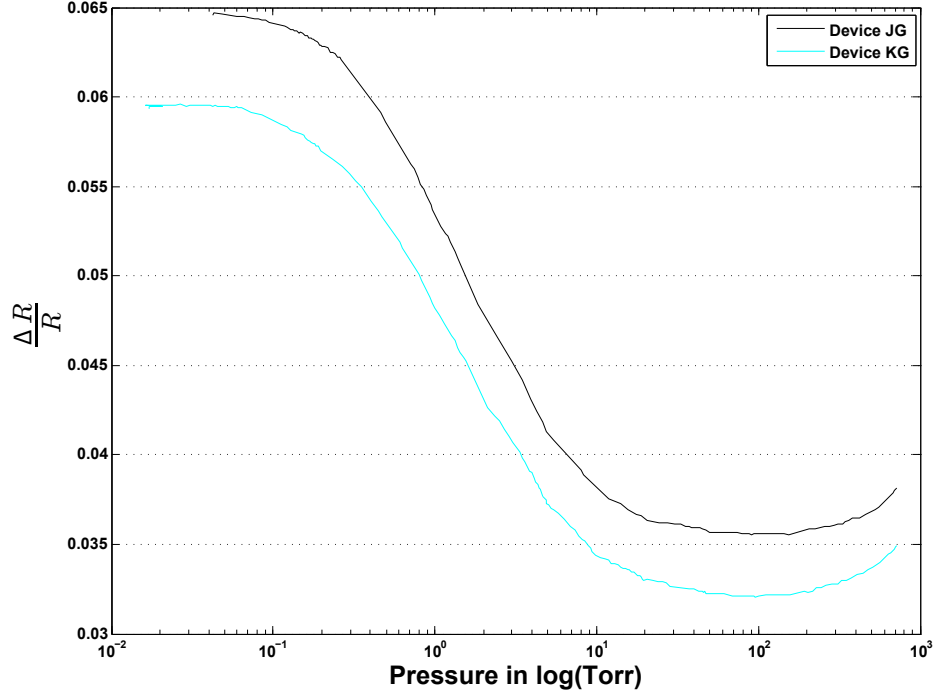
Figure 5.17: $\frac{\Delta R}{R}$ vs. pressure curve for chip CORNER device KG, JG under 100mA current

Table 5.1: Initial resistance change before and after sealing for chip LABC

Device	Before(Ω)	After(Ω)
A	0.659	0.622
B	0.690	0.622
C	0.670	0.618

Table 5.2: Curve shift data for pre-baking and sealing process

Device	Cause of shift	Average $\frac{\Delta R}{R}$ shift
CORNER A	Sealing	0.341
CORNER F	Sealing	0.054
EDGE A	Baking	0.053
EDGE D	Baking	0.105

Figure 5.18: $\frac{\Delta R}{R}$ vs. pressure curve shift before and after sealing process and pressure readout

A characterization curve shift was detected in a sealed sample package. After getting the test point of the sealed sample, the seal was broken and characterization step was done once more to identify the shift in order to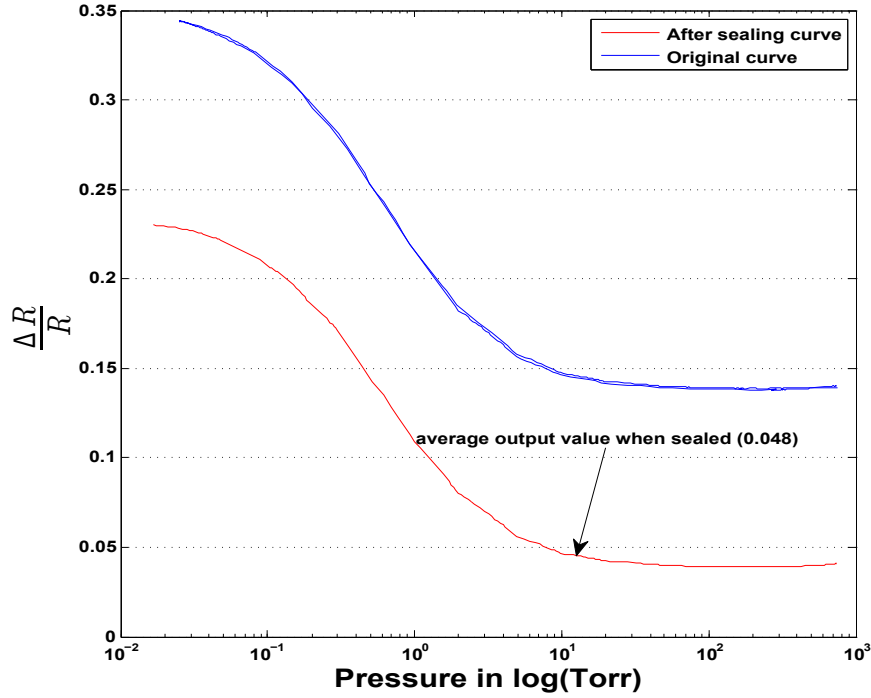 know what pressure was inside the sealed package. As shown in Fig. 5.18, there was a curve shift and the readout pressure was around 13 $Torr$. Both chip LABC and chip CORNER were sealed with our hermetic packaging process described in Section. 4.2.3. For chip LABC at room temperature resistance change was observed after doing test on the sealed package (Table. 5.1). The curve downside shift happened to all bondwire sensors.

Another test was conducted to justify whether the baking step contribute to this characterization curve shift. The chip EDGE was baked for 4 days under $150°C$ but without the sealing step. Curve change shown in Table. 5.2 Characterizing the devices again also gave out a curve shift. That proves the shift is mainly caused by thermal treatments during packaging process. Currently the only way to know the exact pressure inside is to do a break seal test. A number of tests were conducted and results indicated that with a thoroughly pre-baking step with our packaging system the lower bound of the sealing pressure can be pushed to around 1.5 $Torr$.
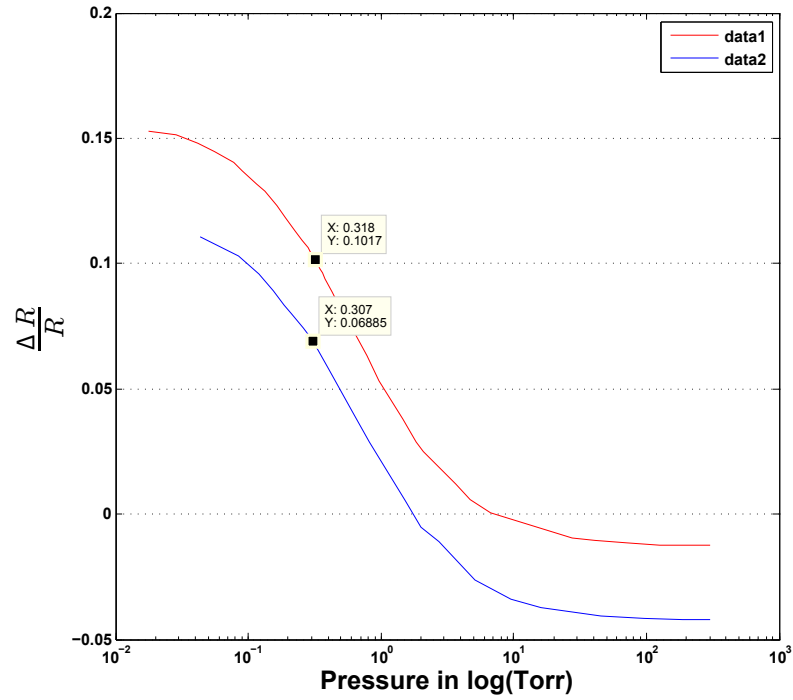
Figure 5.19: Pressure reading with the help of bondwire sensor from packages that sealed with getter material

Our bondwire sensors were also used to test the getter material involved sealing process. As shown in Fig. 5.19, two newly packaged devices shows a pressure about 0.3 $Torr$.

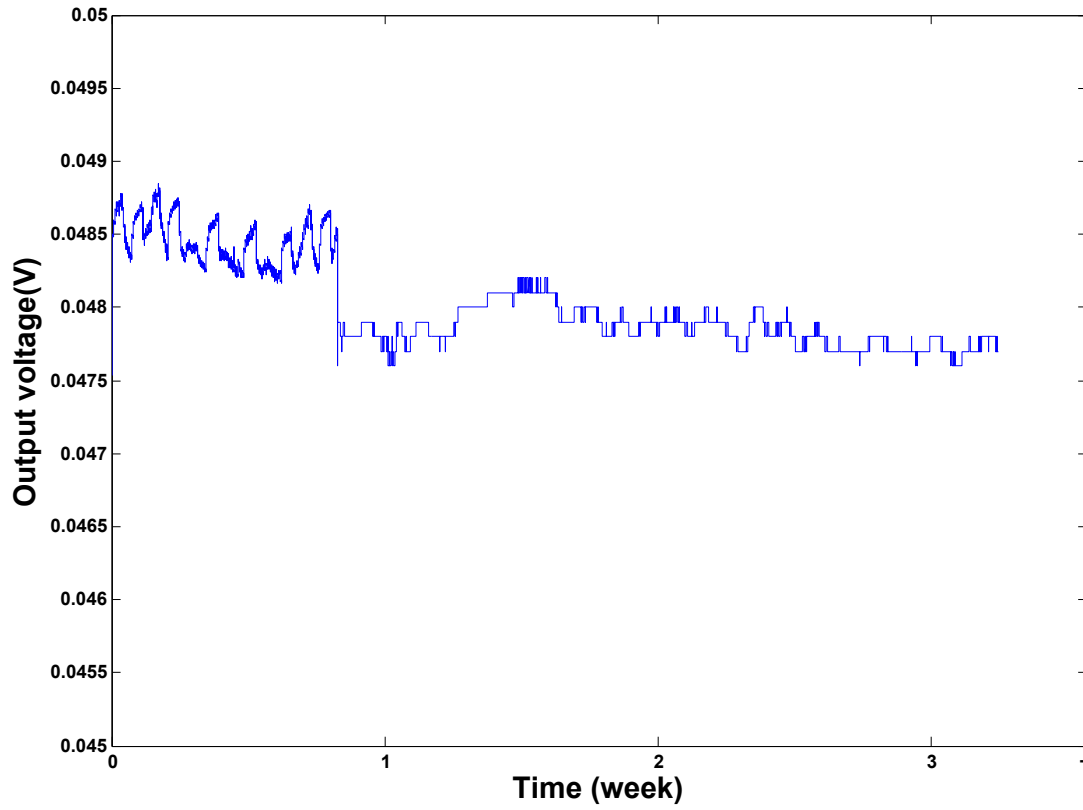## 5.2.4 Hermetic package longterm test

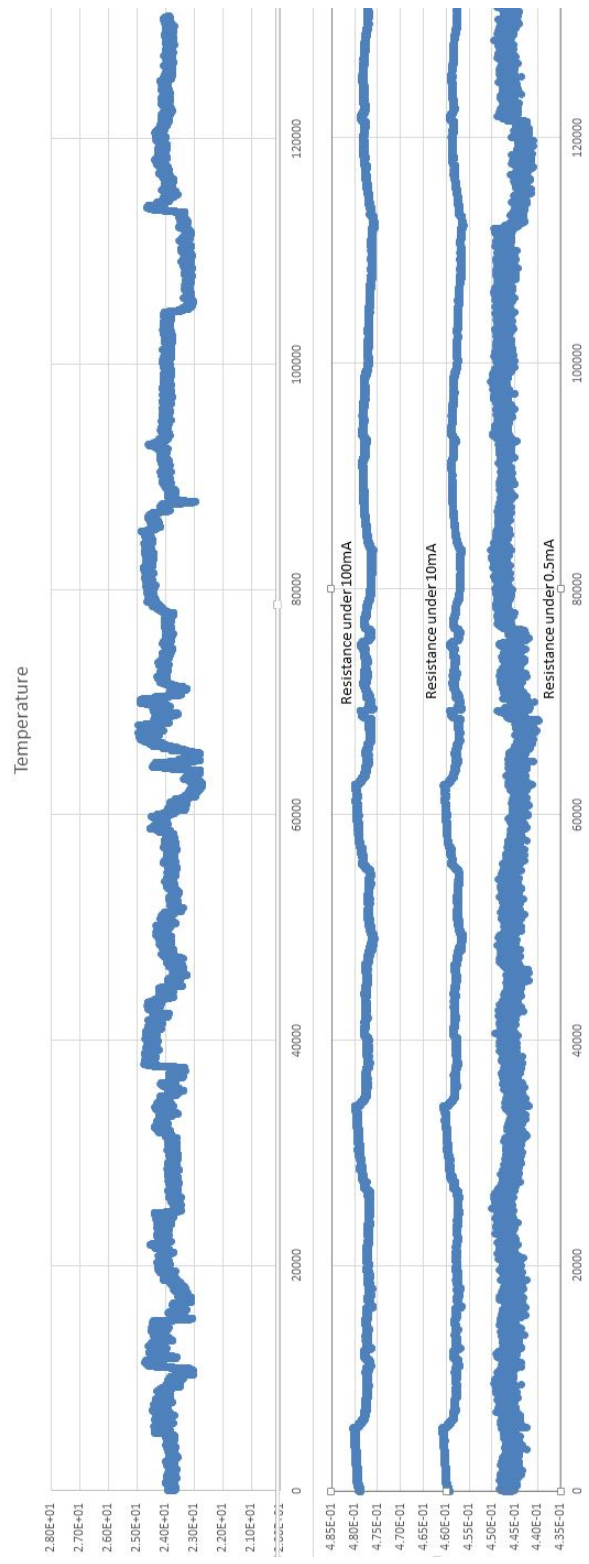Figure 5.20: Longterm test result for chip EDGE after sealing

Figure 5.21: A week's output curve and temperature variation

The reliability of our bondwire sensor and quality of the seal were investigated by longterm monitor. Some devices after encapsulation were kept under testing. Three weeks' of data from chip EDGE device A is shown in Fig. 5.20. The overall data shows a stable seal over nearly a month. Note that after the first week the test was interrupted by one of our colleague. The following data no longer used Keithley as source and switched to Labview programmed data extraction, which caused the inconsistency in figure. Note that there is some kind of pattern inside each week's data. It seems like each day the curve follows the same track but there are also clear distinctions between weekdays and weekends. Our guess of noise source could be ambient temperature and nearby crowd activity. To identify the relationship between ambient temperature and sensor readout, another test with a thermocouple was conducted for a week as shown in Fig. 5.21. The result shows that ambient temperature indeed affects our longterm test's output.

Chapter 6

Conclusions and Future Work

In this chapter, this thesis is concluded by summarizing the research results and contributions. Future research topics are suggested as well.

6.1   Conclusions

An innovative in-package pressure sensing solution for MEMS ceramic package was demonstrated, along with the development of a chip level packaging technique. The feasibility of utilizing the bondwire sensor in real applications was discussed and tested. The advantage of this pressure sensing solution was identified as zero cost, fast speed, space saving and great integrity to any application. The packaging and pressure sensing aim to serve for our extremely sensitive accelerometer.

Review about previous works in hermetic packaging and pressure sensing was summarized. The working principle of the device has been thoroughly illustrated. Simulations for Pirani pressure sensing was achieved with the help of COMSOL Multiphysics solver. The new Pirani bondwire sensor was formed with a regular wedge bonder using commercial gold bonding wire with $1mil$ diameter. A novel method of in-package four point measurement for the first time made the bondwire pressure sensing possible.

Test results for sensor characterization shows a reliable pressure sensing element with dynamic range from 10 $mTorr$ to 50 $Torr$ and good sensitivity. Different layouts of positioning the sensor have been investigated in order to have a flexible sensor alignment. Bondwires that are shorter than 4 mm are proven to have noisy output. The effect of packaging process to sensor output was also studied. It was revealed that the output shift was mainly caused by the thermal treatments during packaging steps. In our application, the main concern focused on environment constancy which is represented by pressure stability. The bondwire Pirani sensor along with the in-package four point measurement is a perfect solution.

On the hermetic packaging side, a chip level packaging process was developed with ATV solder reflow oven. A LCC package was used and eutectic bonding was the main source of our die attachment as well as package sealing. Sealed pressure was measured to be around 1.5 $Torr$ with careful pre-baking process. Packages with getter material deposited was also sealed and tested to expect improved vacuum inside. The ultimate pressure at present can be 0.3 $Torr$ which satisfy most of our applications.

6.2   Future Work

The lower bound of sealed pressure inside the package can still be improved. Currently the pressure value achieved is not as low as it can be. The possible causes could be the contamination inside the packaging oven, the insufficient amount of getter material deposition, or the low temperature activation step.

The output shift as the result of thermal treatment seems to be a main issue for bondwire in-package sensing solution especially in medium or high temperature packaging processes. A possible approach is to do a more thoroughly thermal treatment to in advance push the output shift to its limit before sensor characterization. Then the measurement may yield an absolute reliable prepared reading for sealed packages.

Bibliography

[1] Z. Tao, T. Bobal, M. Oud, and J. Song-Hang, "An introduction to eutectic au/sn solder alloy and its preforms in microelectronics/optoelectronic packaging applications [j]," *Electronics & Packaging*, vol. 8, pp. 2–8, 2005.

[2] N. P. Pham, P. Limaye, P. Czarnecki, V. Olalla, V. Cherman, D. S. Tezcan, and H. A. Tilmans, "Metal-bonded, hermetic 0-level package for mems," in *Electronics Packaging Technology Conference (EPTC), 2010 12th.* IEEE, 2010, pp. 1–6.

[3] J. Chae, J. M. Giachino, and K. Najafi, "Fabrication and characterization of a wafer-level mems vacuum package with vertical feedthroughs," *Microelectromechanical Systems, Journal of*, vol. 17, no. 1, pp. 193–200, 2008.

[4] R. N. Dean, S. Surgnier, J. Pack, N. Sanders, P. Reiner, C. W. Long, R. Fenner, and W. P. Fenner, "Porous ceramic packaging for a mems humidity sensor requiring environmental access," *Components, Packaging and Manufacturing Technology, IEEE Transactions on*, vol. 1, no. 3, pp. 428–435, 2011.

[5] Y. Tao, A. P. Malshe, W. D. Brown, D. R. Dereus, and S. Cunningham, "Laser-assisted sealing and testing for ceramic packaging of mems devices," *Advanced Packaging, IEEE Transactions on*, vol. 26, no. 3, pp. 283–288, 2003.

[6] D. R. Sparks, S. Massoud-Ansari, and N. Najafi, "Chip-level vacuum packaging of micromachines using nanogetters," *Advanced Packaging, IEEE Transactions on*, vol. 26, no. 3, pp. 277–282, 2003.

[7] R. C. Gutierrez, T. K. Tang, C. B. Stell, V. Vorperian, and K. Shcheglov, "Bulk micromachined vacuum sensor," in *Solid State Sensors and Actuators, 1997. TRANS-DUCERS'97 Chicago., 1997 International Conference on*, vol. 2. IEEE, 1997, pp. 1497–1500.

[8] M. Esashi, S. Sugiyama, K. Ikeda, Y. Wang, and H. Miyashita, "Vacuum-sealed silicon micromachined pressure sensors," *Proceedings of the IEEE*, vol. 86, no. 8, pp. 1627–1639, 1998.

[9] C. Mastrangelo, *Thermal Applications of Microbridges.* University of California, Berkeley, 1991. [Online]. Available: https://books.google.ca/books?id=DtBDQAAACAAJ

[10] J. Mitchell, G. R. Lahiji, and K. Najafi, "An improved performance poly-si pirani vacuum gauge using heat-distributing structural supports," *Microelectromechanical Systems, Journal of*, vol. 17, no. 1, pp. 93–102, 2008.

[11] E. S. Topalli, K. Topalli, S. E. Alper, T. Serin, and T. Akin, "Pirani vacuum gauges using silicon-on-glass and dissolved-wafer processes for the characterization of mems vacuum packaging," *Sensors Journal, IEEE*, vol. 9, no. 3, pp. 263–270, 2009.

[12] F. Santagata, J. F. Creemer, E. Iervolino, L. Mele, A. W. Van Herwaarden, and P. M. Sarro, "A tube-shaped buried pirani gauge for low detection limit with small footprint," *Microelectromechanical Systems, Journal of*, vol. 20, no. 3, pp. 676–684, 2011.

[13] Wikipedia, "Pirani gauge — wikipedia, the free encyclopedia," 2015, [Online; accessed 12-November-2015]. [Online]. Available: https://en.wikipedia.org/w/index.php?title=Pirani_gauge&oldid=689153911

[14] C. Zhang, G. Xu, and Q. Jiang, "Characterization of the squeeze film damping effect on the quality factor of a microbeam resonator," *Journal of Micromechanics and Microengineering*, vol. 14, no. 10, p. 1302, 2004. [Online]. Available: http://stacks.iop.org/0960-1317/14/i=10/a=003

[15] J. S. Mitchell, "Low temperature wafer level vacuum packaging using au-si eutectic bonding and localized heating," Ph.D. dissertation, University of Michigan, 2008.

[16] D. Sparks, G. Queen, R. Weston, G. Woodward, M. Putty, L. Jordan, S. Zarabadi, and K. Jayakar, "Wafer-to-wafer bonding of nonplanarized mems surfaces using solder," *Journal of Micromechanics and Microengineering*, vol. 11, no. 6, p. 630, 2001.

[17] Y. T. Cheng, W.-T. Hsu, K. Najafi, C. T. Nguyen, and L. Lin, "Vacuum packaging technology using localized aluminum/silicon-to-glass bonding," *Microelectromechanical Systems, Journal of*, vol. 11, no. 5, pp. 556–565, 2002.

[18] B. H. Stark, Y. Mei, C. Zhang, and K. Najafi, "A doubly anchored surface micromachined pirani gauge for vacuum package characterization," in *Micro Electro Mechanical Systems, 2003. MEMS-03 Kyoto. IEEE The Sixteenth Annual International Conference on*. IEEE, 2003, pp. 506–509.

[19] I. inc. (2015) MEMS-PIRANI pressure microsensor and control software. [Online]. Available: http://www.ino.ca/media/248611/comm-13067_flyer-v2_mems-pirani_with_control_software.pdf

[20] R. R. Tummala, E. J. Rymaszewski, and Y. Lee, "Microelectronics packaging handbook," 1989.

[21] M. A. Schmidt, "Wafer-to-wafer bonding for microstructure formation," *Proceedings of the IEEE*, vol. 86, no. 8, pp. 1575–1585, 1998.

[22] F. Theunis, T. Lisec, W. Reinert, J. Bielen, D. Yang, M. de Jongh, and P. Krusemann, "A novel and efficient packaging technology for rf-mems devices," in *Electronic Components and Technology Conference, 2007. ECTC'07. Proceedings. 57th*. IEEE, 2007, pp. 1239–1245.

[23] A. Garnier, E. Lagoutte, X. Baillin, C. Gillot, and N. Sillon, "Gold-tin bonding for 200mm wafer level hermetic mems packaging," in *Electronic Components and Technology Conference (ECTC), 2011 IEEE 61st*. IEEE, 2011, pp. 1610–1615.

[24] Y. Hirohata, K. Suzuki, and T. Hino, "Gas desorption properties of low-activation ferritic steel as a blanket or a vacuum vessel material," *Fusion engineering and design*, vol. 39, pp. 485–491, 1998.

[25] Y. Tuzi, T. Tanaka, K. Takeuchi, and Y. Saito, "Effect of surface treatment on the adsorption kinetics of water vapor in a vacuum chamber," *Vacuum*, vol. 47, no. 6, pp. 705–708, 1996.

[26] S.-A. Kim, Y. H. Seo, Y.-H. Cho, G. H. Kim, and J. U. Bu, "Fabrication and characterization of a low-temperature hermetic mems package bonded by a closed loop ausn solder-line," in *Micro Electro Mechanical Systems, 2003. MEMS-03 Kyoto. IEEE The Sixteenth Annual International Conference on.* IEEE, 2003, pp. 614–617.

[27] J. Kim, M. Chiao, and L. Lin, "Ultrasonic bonding of in/au and al/al for hermetic sealing of mems packaging," in *Micro Electro Mechanical Systems, 2002. The Fifteenth IEEE International Conference on.* IEEE, 2002, pp. 415–418.

[28] J. Kim, B. Jeong, M. Chiao, and L. Lin, "Ultrasonic bonding for mems sealing and packaging," *Advanced Packaging, IEEE Transactions on*, vol. 32, no. 2, pp. 461–467, 2009.

[29] H. Pham, C. Fan, G. Pandraud, F. Creemer, P. Sarro, N. Van der Pers, P. Visser, and K. Kwakernaak, "Very thin sic membranes for micromachined vacuum sensors," in *Sensors, 2008 IEEE.* IEEE, 2008, pp. 1143–1146.

[30] S. Wang and Y. Feng, "Micro capacitive vacuum sensor based on mems," in *Nano/Micro Engineered and Molecular Systems (NEMS), 2010 5th IEEE International Conference on.* IEEE, 2010, pp. 1160–1164.

[31] C. H. Mastrangelo and R. S. Muller, "Microfabricated thermal absolute-pressure sensor with on-chip digital front-end processor," *Solid-State Circuits, IEEE Journal of*, vol. 26, no. 12, pp. 1998–2007, 1991.

[32] G. Bedö, W. Kraus, and R. Müller, "Comparison of different micromechanical vacuum sensors," *Sensors and Actuators A: Physical*, vol. 85, no. 1, pp. 181–188, 2000.

[33] B. H. Stark, J. Chae, A. Kuo, A. Oliver, and K. Najafi, "A high-performance surface-micromachined pirani gauge in summit vâĎć," in *Micro Electro Mechanical Systems, 2005. MEMS 2005. 18th IEEE International Conference on.* IEEE, 2005, pp. 295–298.

[34] J. Chae, B. H. Stark, and K. Najafi, "A micromachined pirani gauge with dual heat sinks," *Advanced Packaging, IEEE Transactions on*, vol. 28, no. 4, pp. 619–625, 2005.

[35] Y. Qiu, L. Zhao, and Y. Jin, "A novel micro pirani gauge with mono-wire sensing unit for microsystem application," in *Electronic Packaging Technology & High Density Packaging, 2009. ICEPT-HDP'09. International Conference on.* IEEE, 2009, pp. 467–470.

[36] M. Miao, J. Zhang, Y. Qiu, Y. Zhang, Y. Jin, and H. Gan, "A ltcc microsystem vacuum package substrate with embedded cooling microchannel and pirani gauge," in

Nano/Micro Engineered and Molecular Systems (NEMS), 2010 5th IEEE International Conference on. IEEE, 2010, pp. 399–403.

[37] H. Gan, Y. Qiu, M. Miao, and Y. Jin, "A micro in-situ pirani vacuum gauge for microsystem package applications," in *Electronic Packaging Technology & High Density Packaging (ICEPT-HDP), 2010 11th International Conference on.* IEEE, 2010, pp. 125–129.

[38] K. Khosraviani, "Extremely narrow gap surface micromachined pirani pressure sensor," Ph.D. dissertation, Simon Fraser University, 2007.

[39] J. Holman, "Heat transfer, eighth si metric edition," 2001.

[40] C. V. Madhusudana and C. Madhusudana, *Thermal contact conductance.* Springer, 1996.

[41] J. Baker, M. Calvert, D. Power, E. Chen, M. Ramalingam, and T. Lamp, "On the role of the knudsen number with respect to heat transfer in micro-scale flows [in microelectronics circuits]," in *Energy Conversion Engineering Conference, 1996. IECEC 96., Proceedings of the 31st Intersociety*, vol. 2. IEEE, 1996, pp. 1396–1401.

[42] COMSOL, *COMSOL Multiphysics version 4.3b.* The COMSOL Inc., Burlington, MA 01803, 2013.

[43] R. Ghodssi and P. Lin, *MEMS materials and processes handbook.* Springer Science & Business Media, 2011, vol. 1.

[44] S. F. University. (2016). [Online]. Available: http://http://www.4dlabs.ca/

[45] M. Schuettler and T. Stieglitz, "Microassembly and micropackaging of implantable systems," *Implantable Sensor Systems for Medical Applications*, p. 108, 2013.

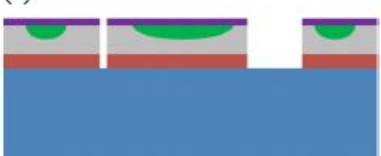# Appendix A

Process Flow for Silicon Pirani Sensor Designs
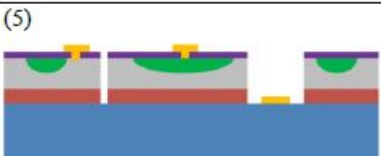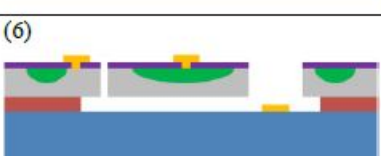
Fabrication step	Description	Mask name	Legend
(1)	Starting silicon-on-insulator (SOI) wafer Device layer thickness: 2 ± 0.5 μm Resistivity: 0.2-1 Ω-cm Box: 0.8μm		■ Device Si ■ Box ■ Handle Si
(2)	Doping process is performed in diffusion furnace followed by a drive-in thermal process at elevated temperatures to create the doped junctions.	Doping	■ Dopant
(3)	The silicon device and nitride layers are etched by Reactive Ion Etching (RIE) to define structures and anchors.	Silicon	■ Si_3N_4
(4)	Contact cuts are etched in the nitride layer to provide electrical connections to the layers underneath.	Contact	
(5)	A lift-off process following sputtering of an Al film defines electrical routings and connections.	Metal	■ Al
(6)	Device is released using a vapour HF step.		

Figure A.1: Process flow of fabrication of silicon Pirani sensor designs

74

Appendix B

Silicon Pirani Sensor Labelling

The following table describes labelling for silicon micromachined Pirani sensors. Determined by the fabrication process, the thickness of device layer is $2\mu m$. All standard straight bridge in our design is of $220\mu m$ length. Horizontal eat sinks were made by device layer as well all surrounding the device design.
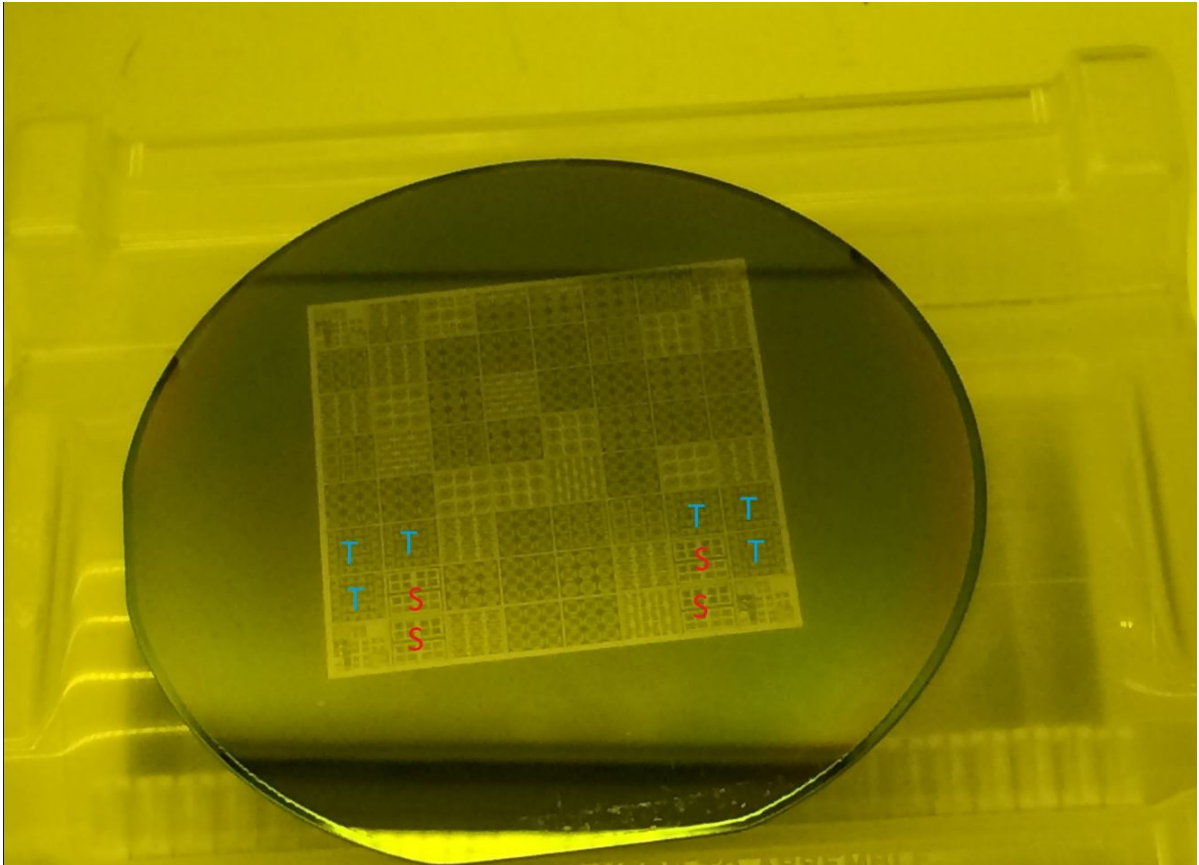
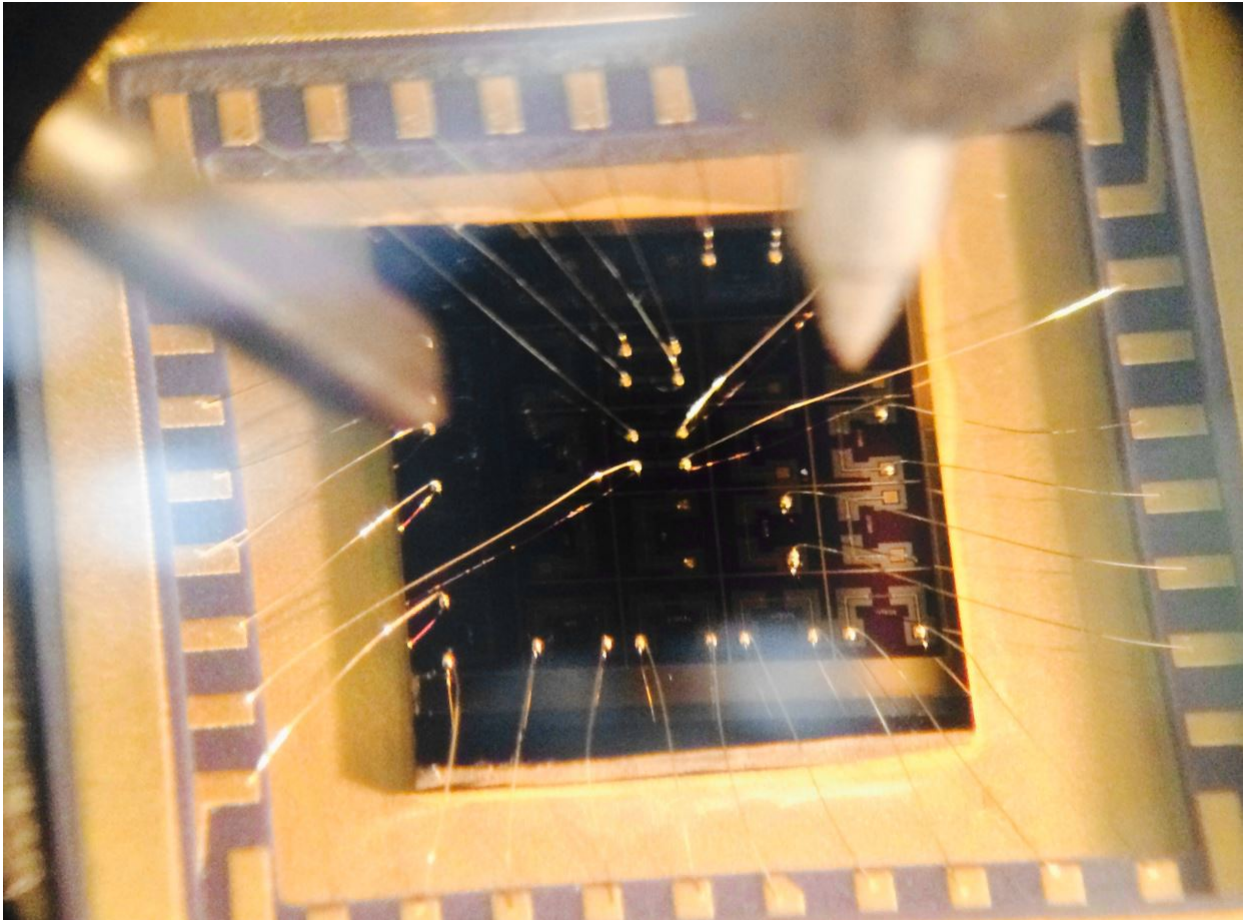Figure B.1: The fabricated silicon die with different device designs

Figure B.2: Picture of wire bonded silicon Pirani sensors

Table B.1: Silicon Pirani labelling

Label	Description
W8	Straight bridge with $8\mu m$ width without heat sink
W8G5	Straight bridge with $8\mu m$ width and $5\mu m$ gap to horizontal heat sinks
W8G10	Straight bridge with $8\mu m$ width and $10\mu m$ gap to horizontal heat sinks
W8G15	Straight bridge with $8\mu m$ width and $15\mu m$ gap to horizontal heat sinks
W16	Straight bridge with $16\mu m$ width without heat sink
W16G5	Straight bridge with $16\mu m$ width and $5\mu m$ gap to horizontal heat sinks
W16G10	Straight bridge with $16\mu m$ width and $10\mu m$ gap to horizontal heat sinks
W16G15	Straight bridge with $16\mu m$ width and $15\mu m$ gap to horizontal heat sinks
SNHS	Serpentine bridge without heat sink
S700	Serpentine bridge with total length $700\mu m$
S1000	Serpentine bridge with total length $1000\mu m$
P50	Bridge with square wing heat sink, length of square $50\mu m$
P50NHS	Bridge with square wing heat sink, length of square $50\mu m$, without heat sink
P100	Bridge with square wing heat sink, length of square $100\mu m$
P200	Bridge with rectangle wing heat sink, length $200\mu m$ and width $100\mu m$
DOPE	Straight bridge surface was partially doped